aerospace

MDPI

Article

Lunar Robotic Construction System Using Raw Regolith: System Engineering

Ketan Vasudeva and M. Reza Emami *

University of Toronto Institute for Aerospace Studies (UTIAS), Toronto, ON M3H 5T6, Canada
* Correspondence: reza.emami@utoronto.ca; Tel.: +1-416-946-3357

Abstract

This paper outlines the system engineering of a Lunar Robotic Construction System (LRCS) for the bagging and manipulation of Regolith Containment Units (RCUs) on the lunar surface. The lunar regolith is the most readily available material on the Moon's surface, which can be utilized for the protection of structures, machines, and equipment from projectiles, thermal variations, and radiation. A mission scenario of employing the LRCS for the creation of a blast berm for landing pads is presented, and the subsystems are subsequently designed in detail. Structural and physical modeling of the LRCS is performed, including simulations of the regolith intake mechanism. An analysis of LRCS mass, power, and cost is also studied, completing its system engineering.

Keywords: lunar construction; robotic construction; in situ resource utilization; lunar regolith; robotic system engineering

1. Introduction

The Moon is now considered by the space community as the most viable base for the future of deep-space exploration, acting as a stepping stone that conveniently mitigates the effects of the Earth's atmosphere and gravity. Works have also begun to investigate the possibility of a cislunar economy, with a particular interest in lunar-derived resources [1,2]. However, the Moon faces some hurdles to regular usage. Humans have not been to the Moon since the Apollo 17 mission in 1972 [3]. This highlights the challenge of our limited experience with and presence on the lunar surface. Space agencies are seeking to address these concerns through technology demonstrations, such as those in the Artemis program, to push toward the development of a sustainable manned lunar base [4]. The European Space Agency (ESA) also conceptualized a Moon Village base [5–8], and the Chinese National Space Administration (CNSA) is working with Roscosmos and 11 other nations to build the International Lunar Research Station [9,10]. The International Space Exploration Coordination Group (ISECG), a collection of 27 space agencies, is a further exemplification of the interest in lunar surface development on a global scale [11]. Most current initiatives to establish a presence on the lunar surface are focused on the lunar South Pole, centering on infrastructure development as well as volatile extraction and processing.

A crucial prerequisite to the lunar bases is the establishment of supporting infrastructure such as berms, shelters, and other protective means for the equipment, machines, and structures. Notably, the establishment of landing pads will be essential to support any sustainable lunar surface infrastructure, due to the fact that the cratering and blast ejecta caused by plumes of the lander engine exhaust hinder the repeatability of lunar landings. The ejecta can reach velocities of over 2000 m/s, traveling large distances in a vacuum,

Check for updates

Academic Editor: Marco Sabatini

Received: 30 March 2026
Revised: 14 May 2026
Accepted: 20 May 2026
Published: 24 May 2026

Copyright: © 2026 by the authors. Licensee MDPI, Basel, Switzerland. This article is an open access article distributed under the terms and conditions of the Creative Commons Attribution (CC BY) license.

potentially entering orbit and damaging surface structures [12]. This makes the creation of blast berms an important task to support sustainable and repeatable lunar landings.

A variety of ISRU-based technologies have been investigated for the creation of such surface infrastructure, leveraging the most readily available resource on the lunar surface, the lunar regolith. The regolith can be used to protect machines and equipment from projectiles, thermal variations and radiation. A comprehensive survey on lunar construction is provided in [13]. Confinement formation, or regolith bagging, is one technology of particular interest, due to the minimal amount of in situ processing required. One study evaluates confinement formation as the best method for building lunar surface structures, with particular strengths in size, in situ ratio, temperature, and production time [14]. Another work also proposes the construction of superadobe structures using regolith bags [15]. Regolith bagging has been previously investigated, as well, by NASA [16,17], including studies at Marshall Space Flight Center (MSFC) to produce garage-like structures [18,19].

This paper is a continuation of a previous work on performing the system-level conceptual design for a Lunar Robotic Construction System (LRCS), which uses raw regolith to fill Regolith Containment Units (RCUs), analogous to terrestrial sandbags, and then manipulates them to create a landing pad blast berm [20]. The LRCS is partitioned into two machines: an RCU Bagger (RB), responsible for filling and bagging RCUs, and a Mobile Manipulator (MM), responsible for placing the RCUs in the environment. The paper begins with detailing the LRCS mission scenario in Section 2. Then, the LRCS concept, including the functional analysis, system requirements, and morphology, is summarized in Section 3. The design of the RCU Bagger, Mobile Manipulator, and general LRCS subsystems is undertaken in Sections 4, 5, and 6, respectively. System-level power, mass, and cost budgeting is discussed in Section 7, and some concluding remarks are made in Section 8. The contributions of this work include continuation of the LRCS design process, system engineering of the RCU Bagger and Mobile Manipulator, initial analyses of the system feasibility, and identification of knowledge gaps that could hinder further concept developments. It should be reiterated that the paper represents the systems engineering of the LRCS concept, using berm stacking as the mission scenario to specify the design. Other mission scenarios or implementations can be similarly conceived for the LRCS concept.

2. LRCS Mission Scenario

The LRCS mission scenario studied in this paper focuses on the construction of a landing pad blast berm. The berm is meant to enable repeatable lunar landings, preventing potential damage caused by the ejecta created by the interaction of plumes of the rocket engine exhaust with the lunar regolith. Simulations have found that the largest and most dangerous ejected particles would travel at hypersonic speeds (over 2000 m/s) at angles up to 3° from the touchdown, while smaller and slower particles would be ejected at angles up to 17° [12,21]. Furthermore, current rocket and localization technologies would require landing pads of up to 100m diameter, which could be reduced to 25 m as landing accuracy improves [22,23]. As such, the LRCS mission scenario considers the protection of surface structures from the most dangerous hypersonic projectiles ejected from landing pads designed for current rocket technologies. To achieve this, the berm will need to be $50 \times tan(3°) \approx 2.6$ m tall. The RCUs may be stacked using either supported or unsupported architectures to achieve the desired height, as shown in Figure 1.

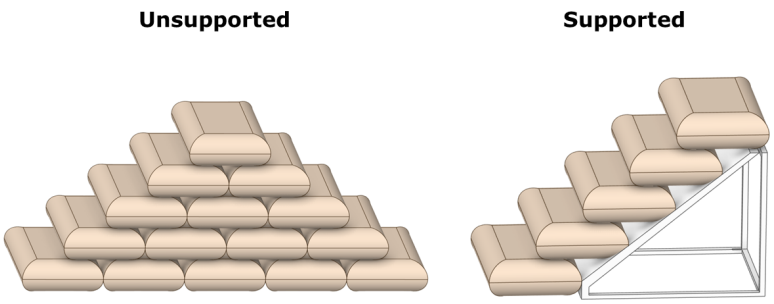

Figure 1. Unsupported and Supported RCU Structures.

This work presents a mission scenario for unsupported RCU structures, but supported structures, using frames built by other systems, would be a practical implementation that could drastically reduce the required number of RCUs while remaining structurally sound. As shown in Figure 2, multiple stacking of RCUs, e.g., double or triple stacking, can be considered to be a modification to simple pyramidal stacking to reduce the amount of RCUs required. The limit for multiple stacking is dependent on the specific structural properties of the RCUs, which should be further investigated. It is anticipated that, due to low gravity as well as the lack of environmental effects (e.g., wind), the RCUs could be stably stacked high with a relatively small base. Other stacking concepts, including asymmetrical stacking or non-pyramidal stacking, would require a more thorough stability analysis considering the non-rigidity of the RCUs and the inter-RCU friction. The number of RCUs for each stacking concept can be determined, starting with simple symmetrical (pyramidal) stacking as a base case, by considering the Gauss series

$$N_{pyramid} = 1 + 2 + \ldots + N_{\text{base}} = \frac{N_{base}(N_{base} + 1)}{2}, \tag{1}$$

where N_{base} is the total number of RCUs in the base row of a single pyramid. Multiple RCU stacking per row can be incorporated such that

$$N_{\text{base}} = \underbrace{\left\lceil \frac{2.6\,\text{m}}{N_{\text{stack}} \times 0.1\,\text{m}} \right\rceil}_{\text{base depth based on desired height}} \tag{2}$$

where N_{stack} is the number of rows with the same amount of RCUs, e.g., single, double, or triple stacked. By substituting Equation (2) into Equation (1) and multiplying by N_{stack}, the total number of RCUs required for a particular configuration would be

$$N_{\text{pyramid}} = N_{\text{stack}} \times \frac{\left\lceil \frac{2.6\,\text{m}}{N_{\text{stack}} \times 0.1\,\text{m}} \right\rceil \left(\left\lceil \frac{2.6\,\text{m}}{N_{\text{stack}} \times 0.1\,\text{m}} \right\rceil + 1 \right)}{2}. \tag{3}$$

Therefore, the total number of RCUs required for the construction of the berm in the various configurations is

$$N_{\text{total}} = \underbrace{\left\lfloor \frac{\pi \times 100\text{m}}{0.43\text{m}} \right\rfloor}_{\text{\# pyramids}} \times N_{\text{pyramid}}\,. \tag{4}$$

In a pyramidal configuration, only the top-most layer has a depth of 1 RCU. Some ballistic testing of lunar regolith has been conducted by NASA, with hypervelocity impact experiments into unconsolidated JSC-1A regolith simulant at incident velocities up to 5.18 km/s showing that the granular target absorbs roughly 75% of the projectile's kinetic energy [24]. However, specific ballistic testing of the RCUs should be performed during

RCU characterization and design, which could further inform operational and deployment scenarios. As a mitigation, surface structures could be kept at a distance from the berm to minimize the structural area protected by only the top-most RCU. To further reduce the operational time, Figure 3 shows the number of required RCUs for the berm as a function of N_{stack}. The greatest challenge with regard to pyramid stability would be disturbances due to the manipulator operations. Therefore, the ability to stack these RCUs repeatably is taken as a requirement for the LRCS manipulator. In this paper, 4 RCUs are taken as a reasonable and achievable stack height, beyond which the reduction in the total number of RCUs is less considerable. Consequently, N_{total} = 81,760 RCUs are deemed to be required for the berm construction. The freestanding ability of the RCUs is supported by Apollo trenching observations, which found that vertical walls of regolith can self-support up to 3 m depth [25]. The loading capacity of the RCUs themselves has been experimentally validated in laboratory testing, with filled Beta® Cloth RCUs sustaining incremental hydraulic press loads up to approximately 1000 kg under Earth gravity (equivalent to a 20 m lunar berm) without observed damage to the bagging material [26]. This indicates that the self-loading of the RCUs is not the limiting factor for the berm height.

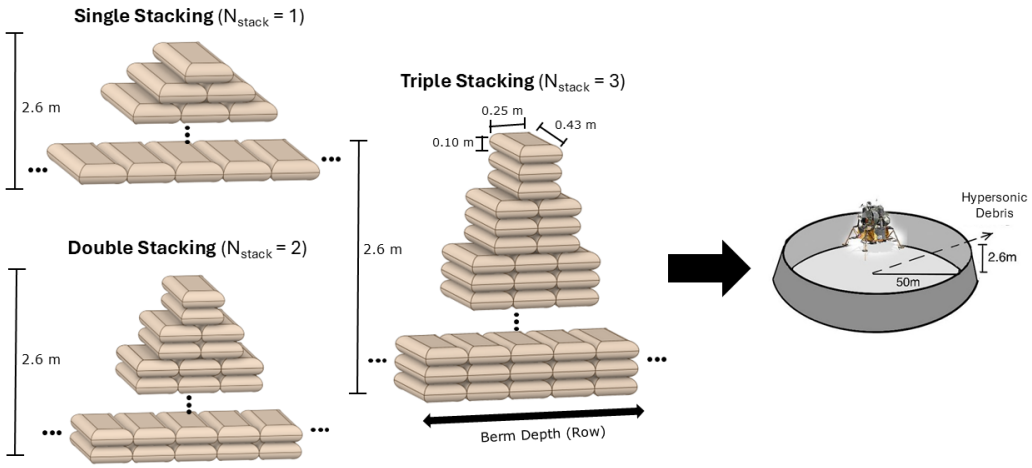

Figure 2. RCU Stacking Methods.

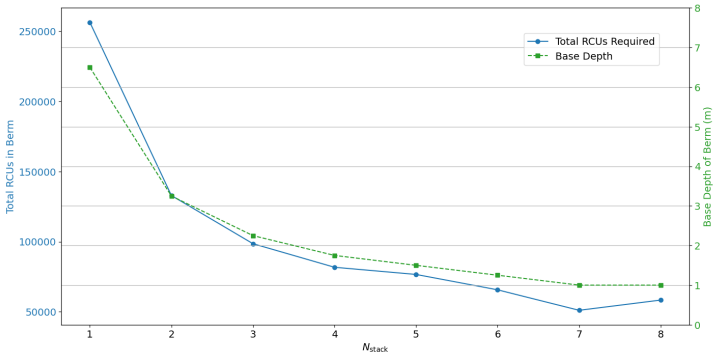

Figure 3. Total Number of RCUs and Berm Base Depth versus Number of Stacked RCUs per Row.

The total amount of regolith required for this process will be M_{total} = 22 kg × 81,760 RCUs = 1,798,720 kg. If the regolith were to be removed from the landing pad area directly, for a highest regolith density of $\rho = 1.92\ \text{g/cm}^3$ [25], the necessary excavation depth (D) would be

$$D = \frac{M_{\text{total}}}{\rho \times A_{\text{landing pad}}} = \frac{1798720\text{kg}}{1920\text{kg/m}^3 \times \pi(50\text{m})^2} = 0.12\,\text{m}\,. \quad (5)$$

The LRCS mission scenario is illustrated in Figure 4. As an initial step, the entire system will need to be delivered to the surface by a lunar lander. Numerous landers are being developed by private companies and space agencies, summarized in Table 1. It is important to note that while landers have distinct mass capacities, they lack specific volumetric constraints, likely due to the fact that the payload bays of the landers are customized for the payloads they carry. The landers have been categorized into light (<300 kg), medium (300–900 kg), and heavy (>900 kg) classes according to their payload capacity. The LRCS has an anticipated total mass of 542.61 kg (see Section 7.2), requiring a medium-class lander.

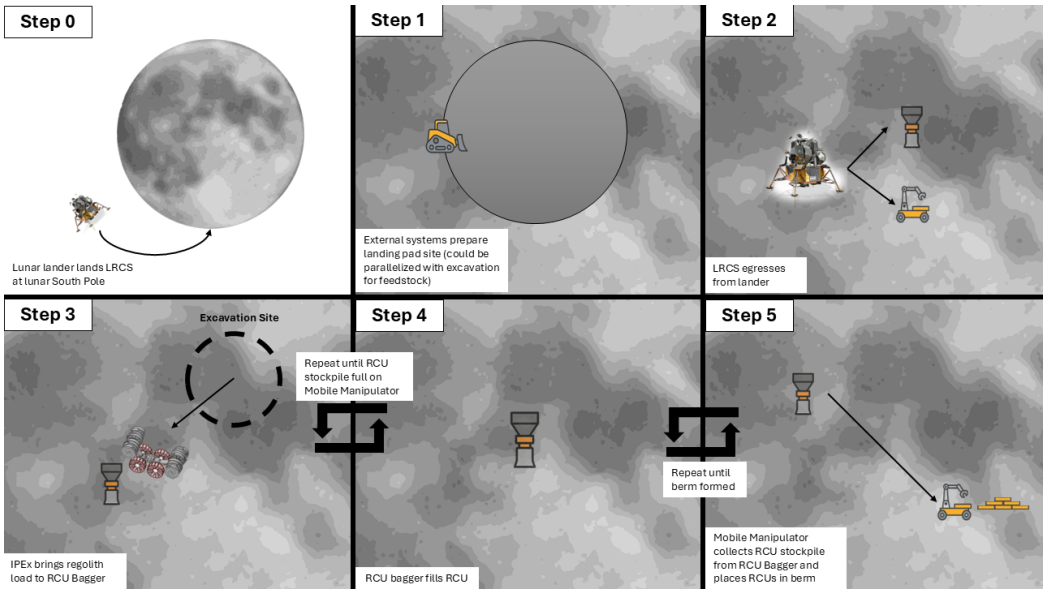

Figure 4. LRCS Mission Scenario.

Table 1. Payload Capacities of Selected Lunar Landers.

Lander	Company	Payload Capacity	Class	Reference
Griffin	Astrobotic	625 kg	Medium	Astrobotic [27]
Peregrine	Astrobotic	120 kg	Light	Astrobotic [27]
Blue Moon Mark 1	Blue Origin	3000 kg	Heavy	Blue Origin [28]
Blue Ghost	Firefly Space	240 kg	Light	Firefly Space [29]
Nova-C	Intuitive Machines	130 kg	Light	Intuitive Machines [30]
Nova-D	Intuitive Machines	1500–2500 kg	Heavy	Intuitive Machines [31]
APEX 1.0	iSpace	300–500 kg	Medium	iSpace [32]
Argonaut	Thales Alenia Space	1500 kg	Heavy	European Space Agency [33]

The landing pad area will need to be prepared as a preliminary step by other robotic systems. This can involve bulldozing and grading the surface, as well as creating the landing pad, although the latter is not required for the LRCS to operate. It is also possible that the site preparation be conducted in parallel with the LRCS operation, since excavation systems may also act as bulldozers and graders, feeding the cleared regolith to the LRCS. Once the landing pad site is prepared, the LRCS operation can begin. As determined by the design conceptualization [20], the LRCS is composed of two separate machines, an RCU Bagger (RB) and a Mobile Manipulator (MM). Considering that a lander has successfully transported the LRCS to the lunar surface near the landing pad location, both machines will need to be offloaded from the lander. Once offloaded, the LRCS will need to initialize its systems, including the deployment of the solar arrays on the RB and MM machines. The LRCS will then traverse to the center of the landing pad location, where the RB will remain for the bagging task. The bagger will then begin producing RCUs, which will be loaded into the MM up to its capacity. This stage relies on an external lunar regolith excavating system

to bring regolith feedstock to the LRCS, namely NASA's ISRU Pilot Excavator (IPEx) [34]. Some of the IPEx properties are listed in Table 2. The excavator will continuously bring regolith to the RB, with a load-dump cycle time of 13.5 min, within which 1 RCU should be created. The IPEx maximum load is 30 kg, and the mass of one RCU is 22 kg. It is approximated that one IPEx load can create one RCU with a 27% margin. Once the MM has filled its stockpile of RCUs, it will traverse to the desired berm location and stack the RCUs using an articulated 4-Degree-of-Freedom (DoF) manipulator. The MM then returns to the RB to collect more RCUs, and the process is repeated until the berm is formed.

Table 2. IPEx Properties (Courtesy: NASA KSC).

Excavation System	Counter-rotating bucket drums
Maximum Traversable Slope	30°
Maximum Obstacle Height	7 cm
Excavator Dry Mass	35 kg
Regolith Capacity	30 kg
Load-dump Cycle Time	13.5 min
Length × Width × Height *	76 cm × 62.5 cm × 68.2 cm

* Stowed configuration—bucket drums up (see Figure 5).

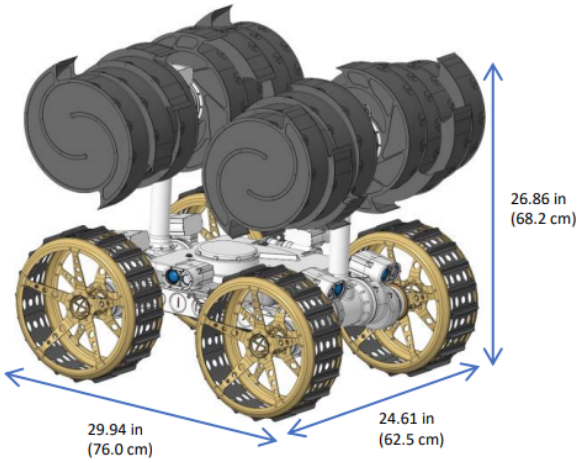

Figure 5. IPEx CAD Model (Courtesy: NASA KSC).

Another important mission-level consideration is the anticipated location on the lunar surface. Most of the proposed habitat locations on the Moon's surface involve the lunar South Pole. For the Artemis Base Camp, NASA has identified 13 candidate landing regions within 6 degrees of latitude of the lunar South Pole [4,35]. NASA cites the presence of water ice and other in situ resources in Permanently Shadowed Regions (PSRs) and long periods of continuous sunlight as major considerations for these selections. Similarly, the ESA's Moon Village project intends to target the Shackleton crater at the lunar South Pole [6,7]. For the ILRS, the CNSA has identified the lunar South Pole as a target habitat location, with researchers paying particular attention to the Amundsen and Malapert craters [36]. The maximum bolometric temperature for the lunar South Pole is shown in Figure 6, illustrating the temperature variability between shadowed regions (craters) and illuminated regions. This indicates the importance of illumination conditions on the operating environment, affecting factors such as temperature and solar power availability. Therefore, the lunar day-night cycle is of particular importance to the LRCS mission scenario. Assuming a mission launch in 2030, the solar illumination conditions for the Shackleton crater, at −89.67° latitude and 129.78° longitude [37], are shown in Figure 7, using ephemeris data from

NASA's SPICE information system for planetary bodies [38]. Please note that a 90° solar incidence angle indicates that the Sun is directly on the horizon, showing that a best-case solar day of approximately 6 months (≈184 days) can be expected.

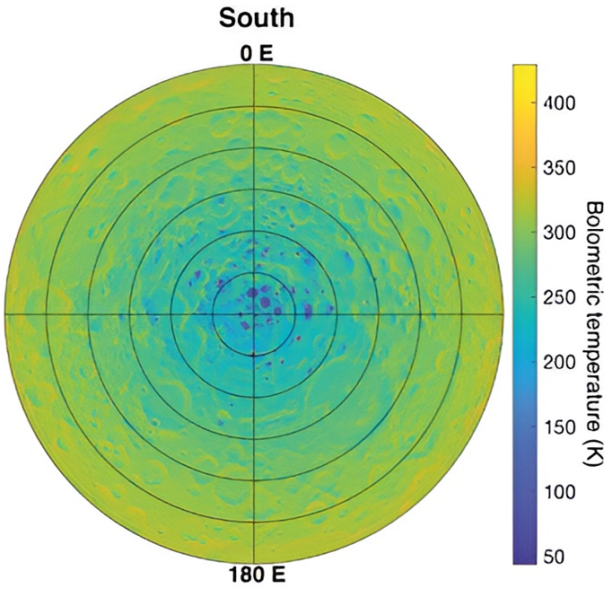

Figure 6. Lunar South Pole Maximum Bolometric Temperature [39].

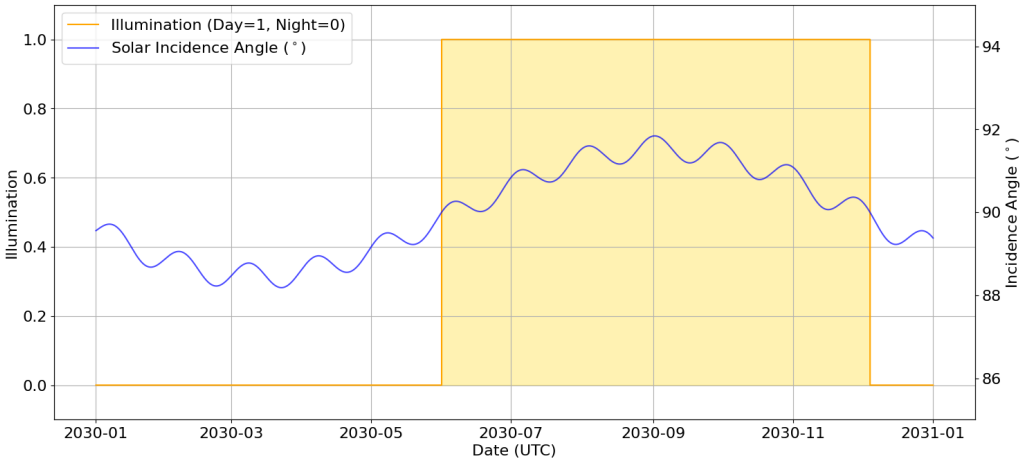

Figure 7. Lunar South Pole Illumination Conditions.

As determined in Sections 4 and 5, the RB has a bagging speed of 44 s/RCU, or approximately 6 min per 8 RCUs, and a maximum traversal speed of 0.2 m/s. The MM has an average RCU placement speed of 84 s/RCU, and a maximum traversal speed of 0.24 m/s, placing 8 RCUs per trip. Various RCU stacking patterns can be considered for creating the berm. A limiting factor for the RCU stacking patterns is the shadow caused by the berm itself. From Figure 7, it is evident that the solar incidence angle is never more than 3° above the horizon, which matches the angle that the fully constructed berm would create with the center of the landing pad. This limits the feasible stacking patterns, since simply constructing the berm around the RB or between the RB and the Sun would require the implementation of a solar array tower at least 2.6 m tall to ensure consistent power generation over the mission duration. Four feasible patterns are considered in Table 3, contrasting estimations for the average RCU placement time, the total duration, and the total power consumption. Some stacking patterns involve moving the RB to follow the MM.

These patterns build the berm in quarters to minimize the amount of movement operations for the RB, during which RCUs cannot be made, and to avoid shadowing the RB's solar panels. Pattern 2 outperforms all the other patterns in every metric. Despite the fact that moving the RB requires some additional energy and bagging downtime, the reduced distance that the MM needs to travel is substantial, resulting in a lower overall duration and power consumption. This stacking pattern results in a stacking rate of approximately 8 RCUs every 25 min. It is important to note that this concept considers the construction of a solid circular berm. In practice, the berm would include a permanent (or actuated) gate to allow for access to the landing pad. This gate should face away from surface structures to prevent accidental ballistic damage.

Table 3. Feasible RCU Placement Patterns.

Pattern	Description	Placement Time (s/RCU)	Duration (Days)	Power (W)
1	The RB remains stationary in the center of the landing pad. The MM builds the berm, but leaves an opening where the Sun can shine onto the RB's solar panels. This opening is closed at the end.	220	208	643
2	The RB follows the MM along a circular path within the landing pad (10 m from berm), building the berm in quarters, starting with the side furthest from the Sun to avoid being shadowed.	190	180	556
3	The RB remains stationary (10 m) outside the landing pad, on the side closest to the Sun. The MM builds the berm, leaving an opening to enter and exit the landing pad area.	242	229	686
4	The RB follows the MM along a circular path outside the landing pad area (10 m from berm), building the berm in quarters to avoid shadowing itself on the side furthest from the Sun.	193	183	564

Note: Time estimates based on average distance to berm and speed. Power estimates based on average case power draw from Section 7.1.

All stacking patterns assume continuous regolith intake from IPEx. Since one IPEx load roughly translates to one RCU created, the duration of the mission is also constrained by the IPEx load-dump time of 13.5 min. Table 4 shows an estimate of the mission duration, using the previously calculated average bagging and placement time per batch of 8 RCUs. The bottleneck with IPEx can be alleviated using multiple IPEx systems. However, the LRCS placement speed becomes the limiting factor once 6 IPEx systems are deployed simultaneously, since 8 RCUs can be produced before the MM is able to collect them. Considering the importance of completing the LRCS berm construction mission within one lunar day, at least 6 IPEx systems would be required for the year 2030 (see Figure 7). This clearly identifies the excavation rate as the limiting factor for the berm building concept. The primary contributors to the mission duration are the excavation rate, the total number of RCUs, and the MM RCU stockpile capacity. The small size of the IPEx system makes it suitable for swarm operations. Also, note that the above estimates are based on the current landing pad diameter of 100 m, which is expected to reduce to a diameter as small as 25 m with the advancement of current technologies.

Table 4. Estimated Mission Duration vs. Number of IPEx Systems.

# of IPEx Systems	Load-Dump Time per IPEx (min)	Estimated Mission Duration (Days)
1	13.50	808
2	6.75	425
3	4.50	297
4	3.38	234
5	2.70	195
6	2.25	177
7	1.92	177
8	1.69	177

3. LRCS Design Overview

The conceptual design of the LRCS is performed in [20], including the development of a functional analysis (see Figure 8) and a set of system-level requirements (see Table A1). The functional analysis and system requirements are used to produce a set of candidate morphologies, based on reference designs, for the four core functional modules of the LRCS, namely intake lunar regolith, deploy empty RCU, interface with and secure RCU, and transport RCU to the desired position and orientation (pose). These core modules constitute the unique design elements for the RB and the MM, as shown in Figure 8, with the other functions and subsystems being shared between the two. The candidates for these modules are assessed using the Analytic Hierarchy Process (AHP) [40], leveraging expert opinions for the prioritization of design criteria. The result of the assessment process for the four functional modules is a system composed of a vibrating funnel for regolith intake, a series of rollers for RCU deployment, a magnet for RCU interfacing, and an articulated 4-DoF manipulator for RCU transport, as illustrated in Figure 9. These morphologies constitute the bases for the subsystem design in Sections 4 and 5.

Since the LRCS will need to manipulate the lunar regolith at scale, it should be considered a dusty system. This is important given the propensity for the lunar regolith to jam and scratch mechanical components, as well as damage electronic components [25]. The LRCS conceptualization finds that reliability, longevity, exposure to dust, and complexity are primary design factors [20]. The system should also minimize power consumption due to limited power availability on the lunar surface.

Some initial material selection should also be considered. As a starting point, Aluminum 6061-T6 is selected for the majority of the structure, due to its relatively high strength-weight ratio [41] and its common usage in many space systems, thus frequently tabled in space system handbooks [42,43]. Furthermore, Aluminum 6061-T6 has been shown to be able to withstand a very wide range of temperatures, performing particularly well at very low temperatures [44], which can be expected on the lunar surface. A thorough analysis of the material properties for Aluminum 6061-T6 can be found in the Metallic Materials Properties Development and Standardization (MMPDS-01) handbook [45], including a density of 2713 kg/m^3. The handbook further suggests a standard thickness range of 0.002–0.005 m for aluminum sheets and tubes. General guidelines for structural design can be taken from NASA's STD-5001B standard: Structural Design and Test Factors of Safety for Spaceflight Hardware [42]. Specifically, the standard suggests a factor of safety of 1.4 for metallic structures. Combining this with the above, a wall thickness of 0.002 m $\times$ 1.4 $\approx$ 0.003 m is considered for the load-bearing elements of the chassis and frame, and 0.002 m for other non-load-bearing structures and plates. Standard Aluminum 6061 plate and tube properties can be found through McMaster-Carr, indicating that 0.002 m-thick plates and 0.003 m-thick 0.025 m $\times$ 0.025 m tubes are reasonable selections [46,47]. After initial loading and thermal analysis, material selection and thickness should be revisited to reinforce high-load areas and consider heat distribution. The design

of the RCUs is not included in this work. Kevlar is used as a material analog wherever the RCU material strength or friction coefficients are considered [17].

Based on these factors, some design guidelines are established for the first iteration of the LRCS, as follows:

Design Considerations for LRCS

- The number of interfaces susceptible to dust ingress, particularly in direct contact with the lunar regolith, should be minimized.
- All rotary shaft interfaces should be protected by Spring-loaded Teflon seals [48].
- All lead-screw mechanisms should have their own housings to prevent jamming along the threads, and interfaces should be protected by Zephyr fiberglass brush seals, clearing excess dust [49].
- The minimal number of motors should be used to actuate all mechanisms.
- All motors should be protected inside sealed housings.
- Aluminum 6061-T6 is used as the primary structural material, with a thickness of 0.003 m for load-bearing structures and 0.002 m for non-load-bearing structures.
- RCUs are made of Kevlar as an analog material.

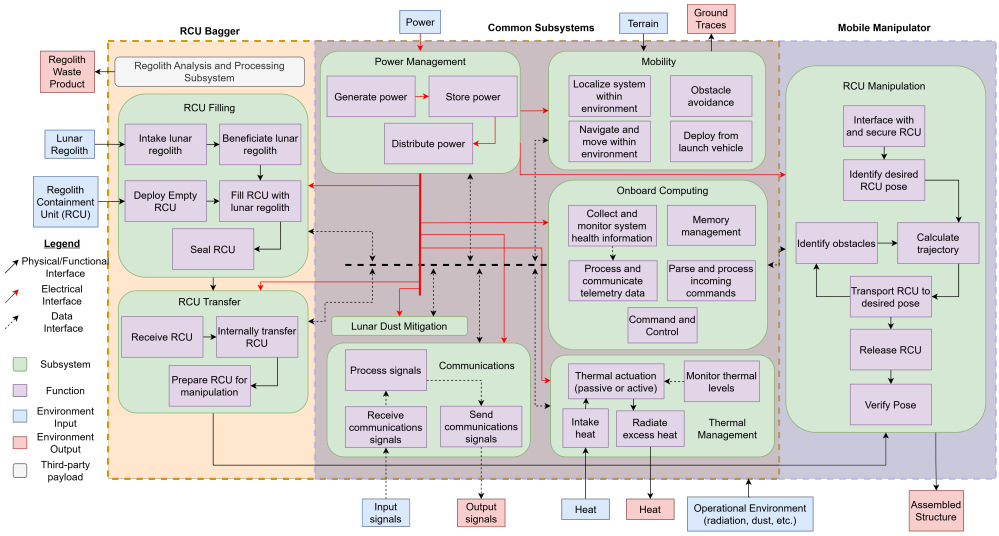

Figure 8. LRCS Functional Analysis.

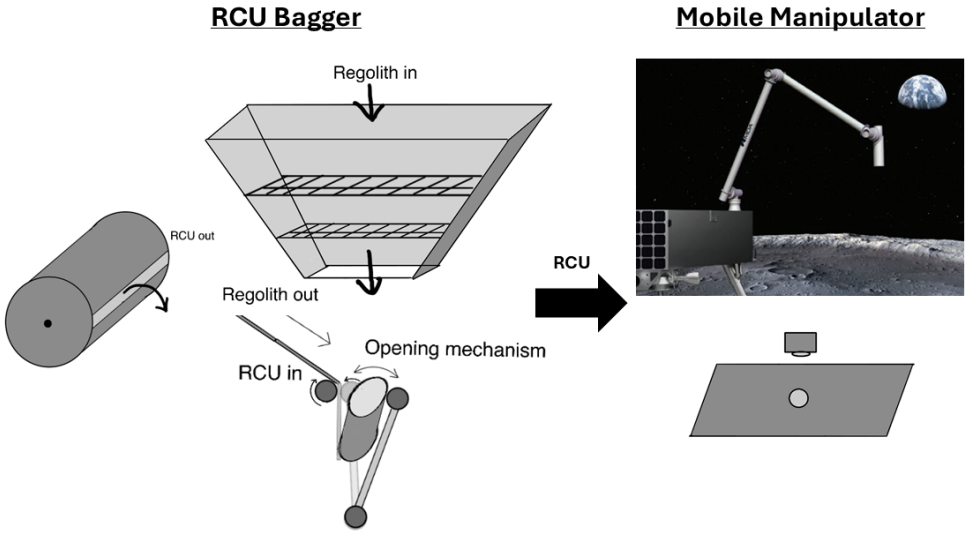

Figure 9. Morphology for Four Primary LRCS Functional Modules.

4. LRCS System Engineering: RCU Bagger

Since the RCU filling and transport tasks are decoupled, the LRCS can be considered as two separate machines: an RCU Bagger (RB) and a Mobile Manipulator (MM). This section focuses on the primary subsystems required for the RB, namely RCU Filling, RCU Transfer, and Mobility. The RCU filling and transfer subsystems are inspired by an automated RCU bagger described in [50], using a series of rollers and hooks to store and open RCUs. Although there exists little further formal research on different methods of RCU bagging, a number of terrestrial industrial bagging systems are also considered in the design [51–57]. Generally, baggers perform either horizontal or vertical filling. The RB performs vertical filling for Form-Fill-Seal (FFS) bagging, allowing gravity to naturally guide the granular lunar regolith into the RCU once its mouth is opened.

4.1. RCU Filling

The RCU Filling subsystem consists of two mechanical assemblies, i.e., the Vibrating Funnel for regolith intake and the RCU bagging mechanism, working together to produce an RCU for manipulation. A 3D-model of the Vibrating Funnel is shown in Figure 10. The dimensions of the funnel opening are constrained by the dimensions of the IPEx bucket wheels (0.625 m × 0.312 m), while the funnel exit is constrained by the dimensions of the RCU (0.43 m × 0.1 m). The funnel exit dimensions assume side filling to minimize the required vertical space, which is important in order to accommodate IPEx's limited dump height (discussed in Section 4.2). Furthermore, the funnel is designed to intake 60 kg of lunar regolith, which is double the capacity of IPEx. Assuming an average lunar regolith density of 1.58 g/cm^3 [25], this represents a storage volume of 60,000 g per 1.58 g/cm^3 ≈38,000 cm^3 (≈0.038 m^3). Considering the entry and exit dimensions, the desired volume, and the geometry of the funnel (trapezoidal prism), a height of 0.185 m is required.

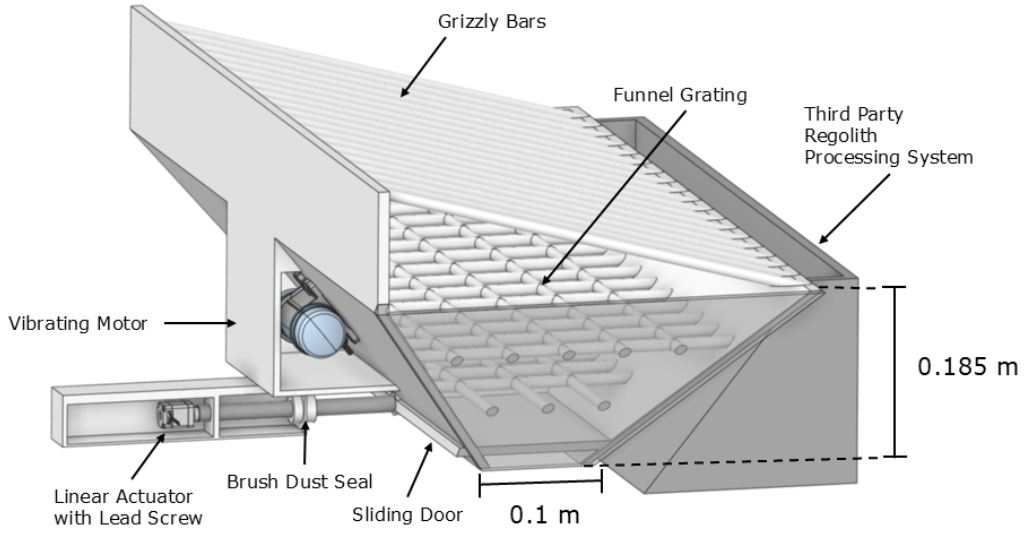

Figure 10. 3D Model of Vibrating Funnel.

Grizzly bars are used for the coarse beneficiation of the lunar regolith, ensuring that rocks larger than 0.04 m in diameter, less than the 0.05 m grating spacing, do not enter the system. These rocks are cleared by vibrating the Grizzly bars at an angle toward a third-party Regolith Analysis and Processing subsystem, supporting science objectives and minimizing wasted materials. A brushless Direct Current (DC) Eccentric Rotating Mass (ERM) vibratory motor is mounted to the wall of the funnel, initially intended to operate at 500 Hz [58]. The purpose of the vibration is to fluidize the lunar regolith, promoting the effective flow through the hopper, as well as preventing its compaction and formation

of arches. The vibration also serves the secondary purpose of clearing the Grizzly bars of excess materials. The necessary vibration amplitude to clear the Grizzly bars can be related to the acceleration a_v due to vibration

$$a_v = A \times (2\pi f)^2 \tag{6}$$

where A and f are the vibration amplitude and frequency, respectively. Clearing can be achieved once

$$a_v \geq g_{\text{Moon}} \times (\sin\theta + \mu_s \cos\theta) \tag{7}$$

where g_{Moon} is the lunar gravitational acceleration (1.625 m/s^2), θ = 14.04° is the angle of the bars, and μ_s is the coefficient of static friction ($\mu_s = 1.211$ between lunar regolith and aluminum [59]). Combining Equations (6) and (7), the vibration amplitude required for displacing excess materials is determined as

$$A \geq \frac{g_{\text{Moon}}(\sin\theta + \mu_s \cos\theta)}{(2\pi f)^2} = 0.233\,\mu\text{m} \tag{8}$$

for f = 500 Hz. The frequency and amplitude of the intake funnel are further investigated using the AGX Dynamics physics-based simulation software for the simulation of the granular lunar regolith [60]. The software is used to produce a granular physics model for representing the lunar regolith's physical and dynamic properties. A simulation of the flow of the granular regolith through the intake funnel is conducted, shown in Figure 11. The objectives of the simulation are to analyze the impact of vibration frequency and amplitude on bulk flow rate and RCU packing density. The simulation considers 22 kg of regolith, composed of 3 mm-diameter particles and 5 cm-diameter rocks, falling in lunar gravity. In Table 5, a grid of frequencies and amplitudes is considered, populated using Equation (8). The simulation finds that a vibration frequency of 500 Hz with an amplitude of 23.3 µm best promotes the bulk flow of regolith. Configurations at 500 Hz appeared to perform best in terms of flow rate, while amplitude had little consistent effect. None of the configurations significantly affected the RCU packing density.

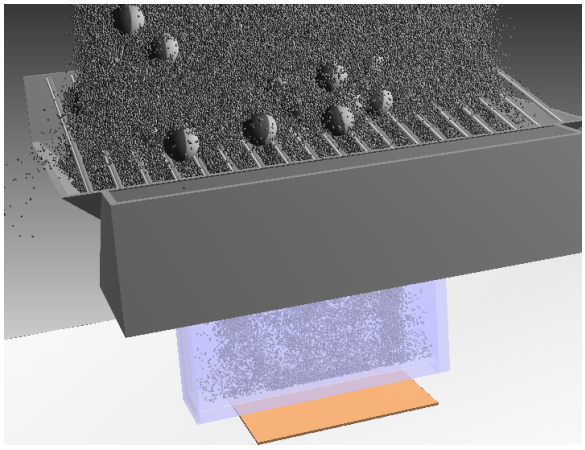

Figure 11. AGX Simulation of Regolith Intake Funnel.

Considering an ERM of mass m_{ERM} at radius r_{ERM}, then the required torque is

$$\tau = (a_v \times m_{\text{ERM}}) \times r_{\text{ERM}} = 0.000115\,\text{Nm} \tag{9}$$

corresponding to a power of

$$P = \tau \times \omega = 0.000115\,\text{Nm} \times 2\pi(500\,\text{Hz}) \approx 0.36\,\text{W}\,. \tag{10}$$

Table 5. Bulk Flow Rate and Packing Density as a Function of Vibration Parameters.

Frequency (Hz)	Amplitude (μm)	Bulk Flow Rate (kg/s)	Packing Density (kg/m^3)
5	0.233	0.533	0.732
5	23.3	0.626	0.754
5	2330	0.522	0.728
50	0.233	0.521	0.740
50	23.3	0.533	0.731
50	2330	0.537	0.725
500	0.233	0.653	0.756
500	23.3	0.786	0.774
500	2330	0.537	0.726

In addition, the funnel exit incorporates a sliding door to enable the start and stop of regolith into the RCU. The door is operated by a lead-screw mechanism, powered by a linear actuator that serves to open the sliding door when the RCU is being filled, and close it once the filling is completed or between operations. The motor and lead screw are intentionally kept outside of the path of the lunar regolith to help prevent dust contamination in the mechanism. To achieve this, the screw is concentrically passed directly along a threaded path within the sliding door, with the outer contact point of the funnel sealed with the Zephyr fiberglass brush seal [48]. The sliding door never opens past the inner funnel wall, keeping the dust and regolith from spreading to the rest of the RB. The open and close conditions are detected by a torque sensor incorporated within the motors of the rollers. This same condition determines whether the vibratory motor should be turned on to avoid the compaction of lunar regolith when the sliding door is closed. The lead-screw and sliding-door mechanisms will need to withstand a maximum load of 60 kg $\times$ 1.625 m/s^2 = 97.5 N in the case that the funnel is completely full of regolith. The sliding door weighs 0.000504 m^3 $\times$ 2713 kg/m^3 = 1.37 kg, requiring a force of 1.37 kg $\times$ 1.625 m/s^2 $\times$ 1.05 = 2.34 N to move, where μ = 1.05 [61] is the aluminum-aluminum coefficient of static friction. The linear actuator will need to produce a torque of [41]

$$\tau = \frac{F \times d_m}{2}\left(\frac{l + \pi\mu \times d_m}{\pi d_m - \mu \times l}\right) \tag{11}$$

where F is the required force , d_m is the diameter of the screw, μ is the coefficient of friction, and l is the pitch or lead of the screw (l = 0.00125 m). Using common handbook values for a 1 cm-diameter lead screw (d_m = 0.01 m), the actuator is required to produce a torque magnitude of 0.014 Nm to move the sliding door.

The RCU bagging assembly, shown in Figure 12, consists of a series of rollers that extract a pre-formed RCU from a roll, move it to an open-mouth configuration below the intake funnel, and then seal the RCU before releasing it to the RCU Transfer subsystem (see Section 4.2). Since the RCUs are side-filled in this configuration, the RCU storage cylinder should measure at least 0.43 m in height. The storage capacity of the cylinder will depend on the properties of the RCUs, such as the thickness of the material, which is not considered in this work, but a cylinder diameter of 0.4 m is nominally decided to match the dimensions of the RB. This outer diameter can be increased to improve the storage capacity. Given a certain RCU thickness t, the capacity of the RCU storage cylinder is

$$N_{RCU} = \frac{D^2_{cylinder} - D^2_{spindle}}{4t^2}. \tag{12}$$

Although the number of RCUs cannot be determined without the thickness, the mass of the roll of RCUs can be estimated using the density of Kevlar (analog material), giving a

mass of $\pi \times (0.2\,\text{m})^2 \times 0.43\,\text{m} \times 1440\,\text{kg/m}^3 \approx 77.8\,\text{kg}$ [62]. The central spindle should be able to wrap at least one RCU, giving

$$D_{spindle} \geq \frac{L_{RCU}}{\pi} = \frac{0.25\,\text{m}}{\pi} = 0.08\,\text{m} \tag{13}$$

as the resulting spindle diameter. Furthermore, the storage cylinder has a set of clamps at one end to enable the replacement of the RCU spindle, so that more RCUs may be loaded into the LRCS. The storage cylinder spindle also has a rotary encoder incorporated to determine how many RCUs have been dispensed.

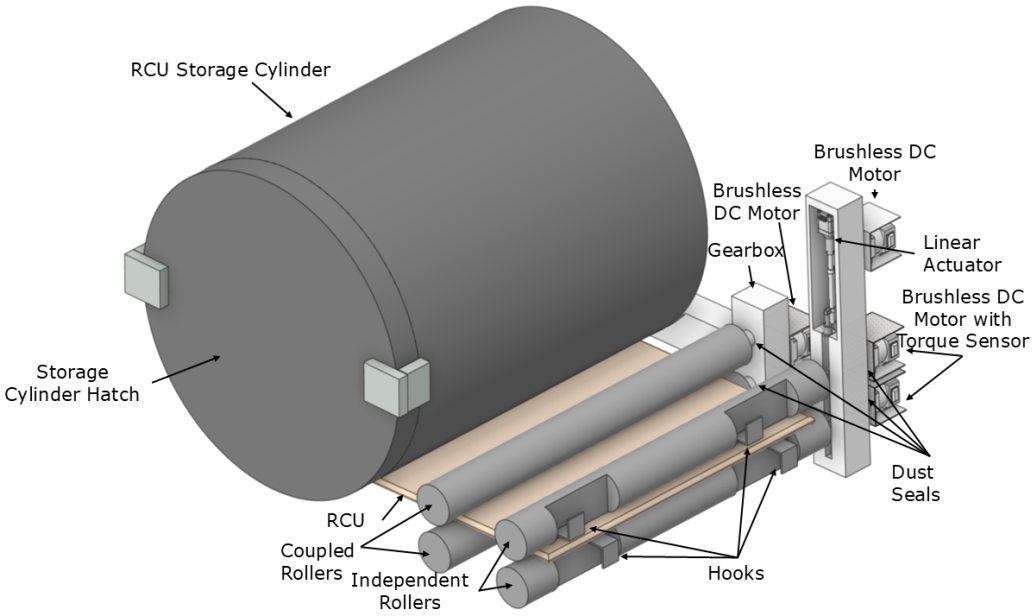

Figure 12. 3D Model of Bagging Mechanism.

Next, there exist two pairs of rollers. The first pair is actuated by a motor that powers a gearbox, resulting in opposite rotations. The diameter of the rollers is set to 5 cm nominally, but should be revisited to account for the RCU material and thickness, ensuring that a sufficient amount of friction is applied. It is also recommended that these rollers be textured to increase the friction between the rollers and the RCU. The second pair of rollers is for opening the RCU using a series of hooks mounted on the rollers, and they are attached to a rotating arm that manipulates the RCU from the storage cylinder to the funnel.

The RCU filling process is shown in Figure 13, and the RCU filling subsystem, with masses and dimensions, is shown in Figure 14. The process begins with the two rollers attached to the storage cylinder pulling out approximately half of the RCU (Step 1, Figure 13). The exact length to be extracted is dependent on the RCU material compliance, but there should be no droop in the material exposed to allow for the second set of rollers to interface with the RCU. Next, the rotating arm brings the two bag-opening rollers to the exposed RCU, and a linearly actuated clamp mechanism brings the rollers in contact with the RCU (Step 2, Figure 13). Then, the rollers rotate so that their mounted hooks grapple the RCU. The gripping action is to engage the hooks with the slotted band mounted on the RCU, as shown in Step 3 of Figure 13. These rollers are independently actuated by two motors, allowing for redundancy if the hooks are not perfectly aligned. During this interfacing, the first set of rollers is locked, allowing the second set of rollers to create a torque during the hooking operation. It is important that the hooks between the rollers be offset to prevent their collision during close operation. At this stage, both sets of rollers are in contact with the RCU. The arm rotates the RCU up to the filling position in two stages (Step 4, Figure 13).

First, it pulls the rest of the RCU through the first passive set of rollers. Then, the first set of rollers locks, applying a holding torque as the arm rips the RCU away from the roll. This tear-away procedure minimizes the need for additional moving parts (e.g., a blade), but will need to carefully consider the design of the tear-away strip to resist the internal friction of the RCU roll.

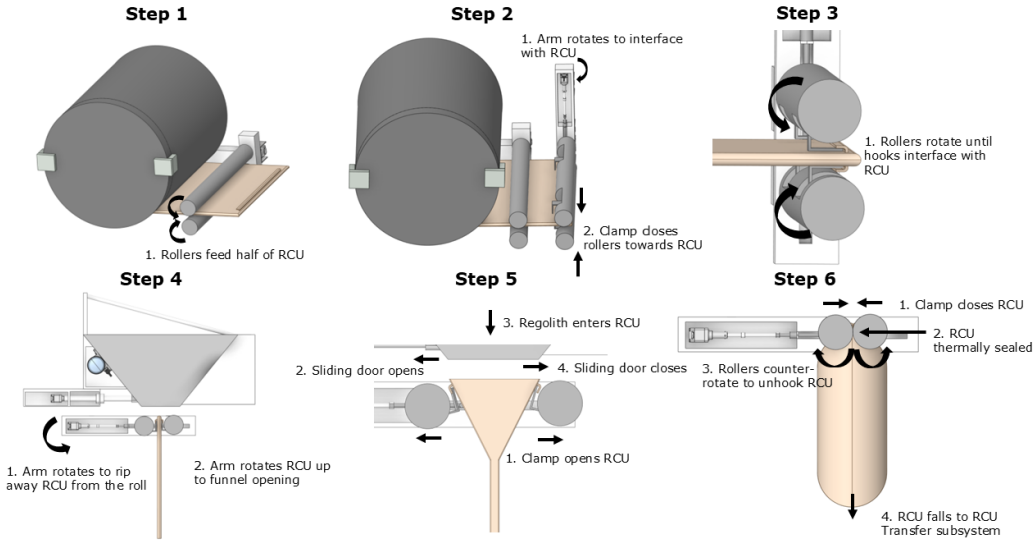

Figure 13. RCU Filling Process.

Now that the RCU is free from the roll, it can be moved by the rotating arm to the filling configuration, directly below the funnel. Once in this position, the clamp mechanism is opened, thereby opening the mouth of the bag (Step 5, Figure 13). At this point, the bag can be filled by opening the sliding door on the funnel and activating the vibration. The stop condition for the filling is detected by weight, using the torque sensors in the rollers. Considering that each roller supports half the weight of the RCU, then

$$\tau_{roller} = \frac{1}{2} r_{roller} W_{RCU} \tag{14}$$

and

$$W_{RCU} = m_{RCU} \times g_{Moon} \,. \tag{15}$$

By combining the two equations, a stop condition can be formed such that filling occurs when

$$m_{RCU} = \frac{2\tau_{measured}}{r_{roller} \times g_{Moon}} \leq 22 \text{ kg} \tag{16}$$

where the 22 kg condition is as determined in [20] for the case of RCU with the largest possible regolith density at $\rho = 1.92$ g/cm^3 [63]. This mass also acts as the loading requirement for the hooks and rollers, meaning that they should be able to withstand as much as 22 kg $\times$ 1.625 m/s^2 = 35.75 N downward force. This force is split between the two bag-filling rollers. Consequently, the required holding torque for one roller is (35.75 N/2) $\times$ 0.025 m = 0.45 Nm. Since this torque is relatively low, the limiting factor for these rollers is likely the resistance to the tear-away force when ripping away the RCU from the roll. More accurate estimates can be determined depending on the specifics of the RCU design. The motor in the arm will also need to hold the RCU, the arm, and the rollers. The force required to move both rollers, each with a mass of 0.44 kg, is 0.88 kg $\times$ 1.625 m/s^2 = 1.43 N. This load is used to quantify the torque required by the linear actuator when the arm is down (Step 2, Figure 13), using Equation (11) with the

same parameters and finding a torque value of 0.0081 Nm. The force required to move the arm is 0.36 kg × 1.625 m/s^2 = 0.59 N. Combining the moments for these forces, the torque required by the motor should be no less than (35.75 N × 0.15 m) + (0.44 kg × 1.625 m/s^2 × 0.1 m) + (0.44 kg × 1.625 m/s^2 × 0.2 m) + (0.59 N × 0.1 m) = 5.64 Nm when the arm is horizontal. Furthermore, the linear actuator in the arm will need to withstand a 35.75 N + 1.43 N = 37.18 N downwards force on the lead screw when the arm is horizontal.

Once the filling is completed, the clamp mechanism closes and an element inside the roller is electrically heated, thermally sealing the RCU (Step 6, Figure 13). The specifics of the thermal sealing process, such as melting temperature, are dependent on the RCU material and whether a thermal heating strip is sewn into the RCU. However, the sealing could be achieved by a Nichrome wire element, the power for which can be found using the resistance and voltage,

$$P = \frac{V^2}{R} = \frac{V^2}{\rho L / A} \quad , \tag{17}$$

where ρ is the resistivity of Nichrome, L is the length of the strip, and A is the cross-sectional area of the strip. Considering some strip of thickness 0.0001 m, width 0.01 m, and length 0.5 m, with a resistivity of 1.09 × 10^{-6} Ωm [64], operated at a voltage of 15 V, an estimated power of 413 W is obtained. Now that the RCU is sealed, the rollers rotate in the opposite direction, unhooking the RCU and allowing it to fall onto the RCU Transfer subsystem, further detailed in Section 4.2. The time required for the bagging process in Figure 13 is estimated in Table 6. Since the anticipated torque rating of the actuators far exceeds the required torques (see Section 4.4), and actuator RB motor operations do not carry significant loads, average speeds of 40°/s and 0.1 m/s are considered for the rotary and linear actuators, respectively. Furthermore, an estimate of funnel flow rate can be formulated by scaling the outlet surface area of a funnel experiment conducted in lunar gravity and vacuum conditions [65]:

$$\dot{m}_{\text{Funnel}} = \frac{l_{\text{Funnel}} \times w_{\text{Funnel}}}{l_{\text{experiment}} \times w_{\text{experiment}}} \cdot \dot{m}_{\text{experiment}} = \frac{0.43\ \text{m} \times 0.1\ \text{m}}{0.015\ \text{m} \times 0.018\ \text{m}} \cdot 0.72 \frac{\text{kg}}{\text{min}} = 114.7 \frac{\text{kg}}{\text{min}}. \tag{18}$$

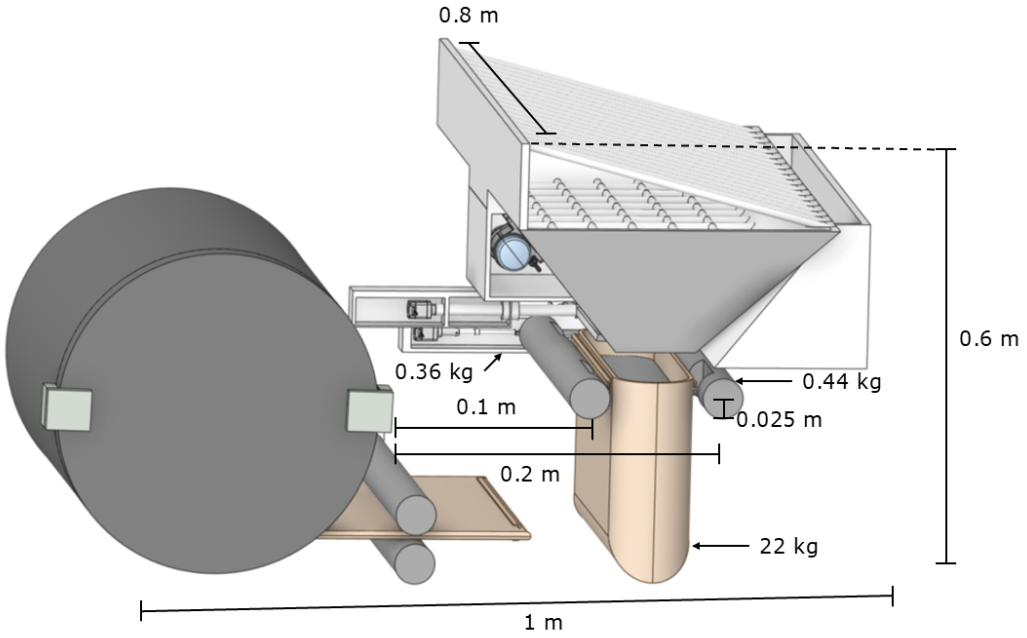

Figure 14. 3D Model of the LRCS RCU Filling Subsystem.

Table 6. LRCS Bagging Process Time Estimation (see Figure 13).

Steps		Time (s)
Step 1		
	Step 1.1—Rollers feed half an RCU	5
Step 2		
	Step 2.1—Arm rotates to interface with RCU	2.25
	Step 2.2—Clamp closes rollers towards RCU	0.5
Step 3		
	Step 3.1—Rollers rotate until hooks interface with RCU	6.75
Step 4		
	Step 4.1—Arm rotates to rip away RCU from roll	0.25
	Step 4.2—Arm rotates RCU up to funnel opening	2
Step 5		
	Step 5.1—Clamp opens RCU	0.5
	Step 5.2—Sliding door opens	1
	Step 5.3—Regolith enters RCU	16
	Step 5.4—Sliding door closes	1
Step 6		
	Step 6.1—Clamp closes RCU	0.5
	Step 6.2—RCU thermally sealed	3
	Step 6.3—Rollers counter-rotate to unhook RCU	4.5
	Step 6.4—RCU falls to RCU Transfer subsystem	1
	Total Time	**44 s**

4.2. RCU Transfer

The RCU Transfer subsystem, shown in Figure 15, is closely related to the RCU Filling subsystem, interfacing with it to collect the sealed RCU and move it out of the system to a position where it can be manipulated. Considering the design of the RCU Filling subsystem (see Section 4.1), a mechanism is required to move the RCU from underneath the Vibrating Funnel. In traditional industrial bagging, this is typically achieved by a conveyor. Although a non-powered conveyor that leverages gravity would be ideal, the LRCS is constrained in the vertical dimension by the height of IPEx (see Figure 5). In fact, the maximum dump height of IPEx can be estimated by considering the angle required for the clearance of the 31.2 cm-diameter bucket drums over the wheels of equal dimension. Considering that only half a bucket drum would need clearance from the wheel axle height (due to the dumping pattern), it can be found that IPEx has a maximum dump height of (Figure 5)

$$\underbrace{(0.682\,\mathrm{m} - 0.156\,\mathrm{m})^2}_{\text{bucket drum actuator length}} - \underbrace{\left(\frac{0.312\,\mathrm{m}}{2}\right)^2}_{\text{wheel radius}} - \underbrace{\frac{0.312\,\mathrm{m}}{2}}_{\text{bucket drum radius}} = 0.346\,\mathrm{m}\,. \tag{19}$$

Comparing the maximum dump height with the total height of the RCU Filling subsystem in Figure 14, it is evident that IPEx will require additional dumping height to successfully dump its load into the LRCS. This motivates the addition of a ramp to the RB, the maximum angle of which is 30° according to Table 2. The final height for this ramp will be determined according to the combined height of the RCU Filling and RCU Transfer subsystems. The limited vertical space necessitates the implementation of a powered conveyor for the RCU Transfer subsystem.

Conveyors have been proposed for the movement of lunar regolith, with analogies being drawn to dusty ore mining environments [48,66]. However, the materials used in traditional conveyors, e.g., rubber, are not suitable for the lunar environment due to temperature variations. Alternative conveyors, such as chain-link, suffer from jamming under

dust exposure and require frequent maintenance. Another option is the implementation of a lead-screw mechanism, but this requires too long a screw to push along the length of the bag, and the threads would be under constant dust exposure, leading to jamming. Therefore, a simple lever arm is implemented to push the RCU out of the system along a chute, using a motor with an Aeroflex dust-tolerant seal. The required force and subsequent torque can be calculated by considering the force required to overcome the static friction of the chute. Using a coefficient of static friction of 0.18 [67], assuming an aluminum chute and Kevlar as the RCU material, a force of at least 22 kg $\times$ 1.625 m/s^2 $\times$ 0.18 = 6.44 N must be enacted on the RCU. This corresponds to a torque of 6.44 N $\times$ 0.25 m = 1.61 Nm. Additionally, the chute has sloped walls to align the RCU as it falls from the rollers. The chute is designed to accommodate one extra RCU, sticking out of the RB by one RCU length for the MM to collect.

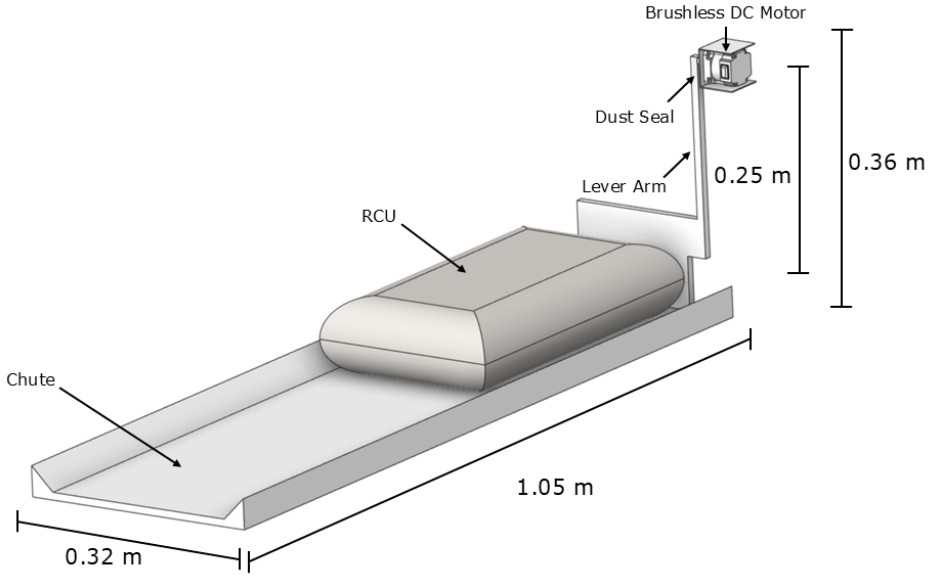

Figure 15. 3D Model of RCU Transfer Subsystem.

4.3. RCU Bagger Mobility

The RCU Bagger requires a Mobility subsystem that will deploy it from the launch vehicle and allow it to displace itself in the environment. The RB can be displaced by a simple set of differentially steered wheels under the primary supports. Since the bagger does not require a high displacement speed, field-tested wheels designed for the lunar surface can be implemented, such as the wire mesh wheels developed by NASA and General Motors [68]. Furthermore, these wheels will not be required to traverse complex terrain, since the RB will primarily operate within the landing pad area. Therefore, it is reasonable to assume a maximum obstacle traversal height of 0.07 m, similar to IPEx (see Table 2). Continuing to take IPEx as a reference design, wheels of approximately 0.3 m in diameter should be able to achieve this obstacle clearance. The mass of each wheel can be scaled from the original Lunar Roving Vehicle (LRV), giving a mass of 2.02 kg per wheel. The wheels are to be individually actuated by 4 motors. To quantify the torque required by the motors, we can find the force required to move the system of mass $m = 197.98$ kg forward at the speed of v = 0.2 m/s (similar to MM) on terrain with maximum grade of $\theta = 30^\circ$ (similar to IPEx) and for a conservative rolling resistance of $\mu_r = 0.02$ [25], reaching the top speed in t = 5 s

$$F_{total} = mg\mu_r \cos(\theta) + mg \sin(\theta) + m\frac{v_{desired}}{t_{acc}} \approx 174\,\text{N}.$$

Consequently, the required torque per motor would be (r_{wheel} = 0.15 m)

$$\tau = \frac{F_{total}}{4} \times r_{wheel} = 6.5\,\text{Nm}\,. \tag{20}$$

Note that the mass of the system is estimated based on a combined mass of 78 kg for the solar panels and batteries prior to sizing (see Section 7.1).

The RB must also consider some sensors to enable localization and traversing in the workspace. However, since the RB does not require detailed environmental mapping, this is achieved using a classical stereo camera apparatus with two optical cameras. These are mounted on top of the RB using a mast, allowing for a clear view of the surroundings. Furthermore, the mast has two degrees of freedom, with a 360° planar view of the environment and a 180° vertical range, allowing it to both view the environment as well as inspect the RB for jamming, damage, or faults. This setup is similar to that of Perseverance's Mastcam-Z stereo cameras, which are used as a reference design [69]. The RB also implements an Inertial Measurement Unit as a standard input for most dead-reckoning and localization algorithms, which will be kept close to the other Onboard Computing architecture (see Section 6.1). Figure 16 shows the RB Mobility subsystem along with the chassis.

4.4. RCU Bagger Overall Design

The final design for the RCU Bagger, including the primary subsystems and plating, is shown in Figure 17. The figure does not include the Power, Onboard Computing, or Communications subsystems, which are further detailed in Section 6. Please note that the RB structure does not seal the system, to allow the dust to escape, but individual components are sealed against the dust. Now that the primary subsystems of the RB have been determined, it is possible to find the height of the ramp for IPEx, as mentioned in Section 4.2. The height from the ground to the funnel opening is 0.7 m. Considering that IPEx's dump height is approximately 0.35 m (see Section 4.2), with an additional 0.05 m margin, and assuming a ramp that is angled at IPEx's maximum traversal slope of 30° (see Table 2), a ramp length of 0.9 m is determined. This ramp is actuated so that it can be stowed during traversal and deployed during intake. The ramp is actuated by a single motor, and must withstand a 35 kg × 1.625 m/s^2 × cos(30) = 49.3 N normal force from IPEx. Assuming a 0.03 m (load-bearing) thick Aluminum 6061-T6 ramp of density 2713 kg/m^3, the mass of the ramp is estimated to be approximately 1.96 kg. Consequently, the ramp motor must be able to produce 1.96 kg × 1.625 m/s^2 × 0.4 m = 1.3 Nm of torque. To verify the stability of the ramp under the IPEx load, we need to ensure that

$$\sigma_{bending} = \frac{Mc}{I} \leq \frac{\sigma_{yield}}{\text{Safety Factor}} \tag{21}$$

where $M = FL/4$ being the bending moment for a for a force F = 49.3 N applied to a simply supported beam of length L = 0.9 m, c = 0.0015 m being the distance to the neutral axis (half the plate thickness), and $I = wt^3/12$ being the moment of inertia for a rectangular plate of width w = 0.14 m and thickness t = 0.003 m. Taking $\sigma_{yield} = 241.3\,\text{MPa}$ [47] and safety factor of 1.4 [42],

$$\sigma_{bending} = 13.2\,\text{MPa} \leq \frac{241.3\,\text{MPa}}{1.4} = 172.4\,\text{MPa}\,, \tag{22}$$

which is well below the yield stress for the ramp.

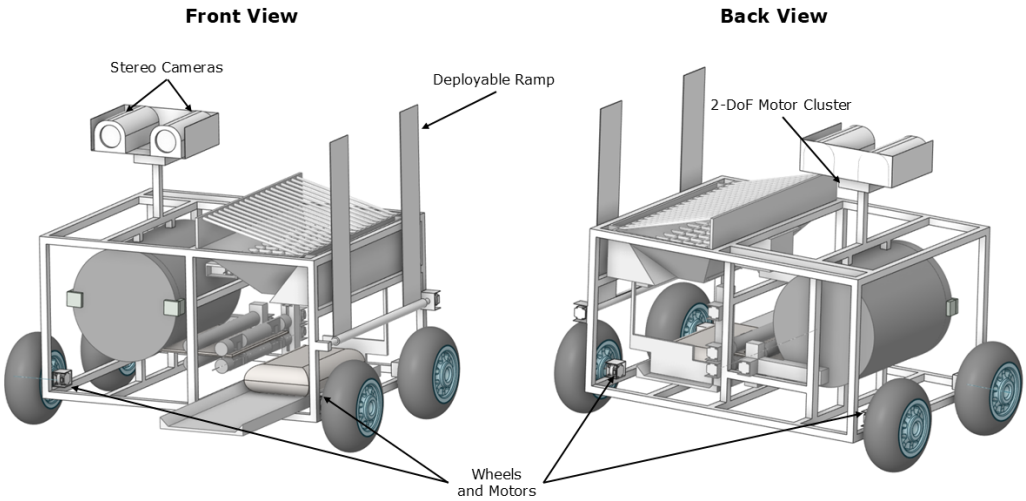

Figure 16. 3D Model of RCU Bagger Chassis, Mobility Subsystem, and Deployable Ramp.

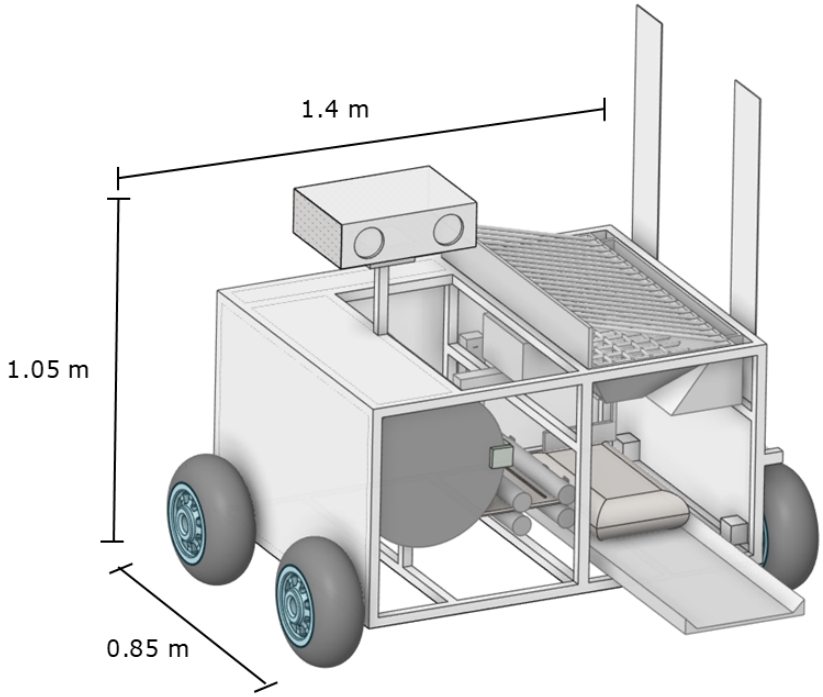

Figure 17. 3D Model of RCU Bagger.

Only a few actuators have been built that could survive the lunar environment, such as those used in COLDArm [70], which is a lunar manipulator designed to operate in temperatures ranging from 93 K to 373 K with no additional survival heaters. Therefore, the COLDArm motors are considered to be the baseline for the RB actuators. The COLDArm brushless DC motors can function on the lunar surface, and are rated for a torque of $\tau_{\max} = 98$ Nm at a mass of 1.4 kg per actuator, exceeding the necessary capabilities of all actuators, even considering conservative factors of safety. The COLDArm actuators operate on a 28 V power rail, and can draw up to 2 A of current, implying a peak power draw of $P_{\max} = 56$ W. Since torque and current are directly proportional, this can be scaled linearly to estimate the average power draws of the actuators in the system for the Power budget in Section 7.1, so that

$$P(\tau) \approx P_{max}\left(\frac{\tau}{\tau_{max}}\right). \tag{23}$$

The RCU Bagger chassis is shown in Figure 16, including the Mobility subsystem and deployable ramp. The chassis is designed to support the load-bearing elements of the RB, such as the RCU storage cylinder, the funnel, and the RCU Transfer subsystem chute. All motors have attachment points on the chassis for stability. Furthermore, a basic structural analysis of the chassis is performed using the Finite Element Analysis (FEA) in ANSYS 2025. The result of the FEA analysis is shown in Figure 18, indicating structural stability under lunar gravity. The FEA demonstrates that no stress values approach the yield strength of 241.3 MPa for Al 6061-T6. In addition, the FEA indicates anticipated deformations under 0.24 mm, well below the limits. The highest loads are experienced directly under the RCU storage cylinder, as expected for the heaviest element in the system.

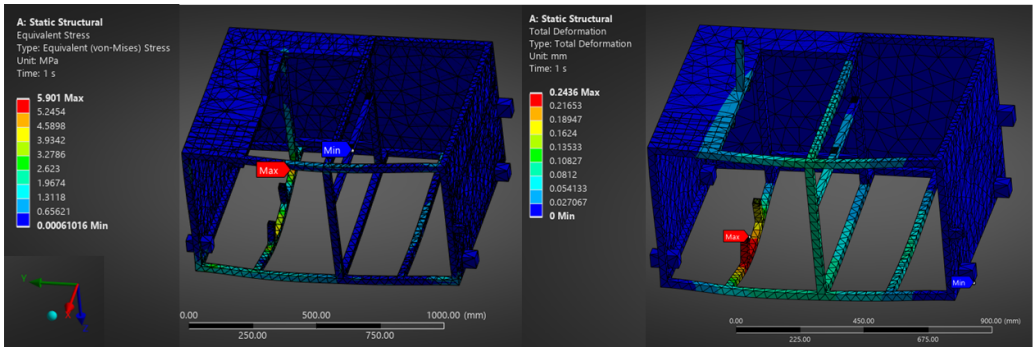

Figure 18. Stress and Deformation Model of RB in Lunar Gravity.

5. LRCS System Engineering: Mobile Manipulator

The second machine of the LRCS is the Mobile Manipulator, shown in Figure 19, which uses an articulated 4-Degree-of-Freedom (DoF) manipulator to collect RCUs from the RCU Bagger, transports them to the berm location, and then places them into the berm. The MM takes inspiration from similar systems, namely GITAI's Lunar Rover [71,72] and MDA's Skymaker. These two solutions combine well, since GITAI's Lunar Rover is a mobility system created for the lunar environment and is already designed to operate with manipulators of similar size.

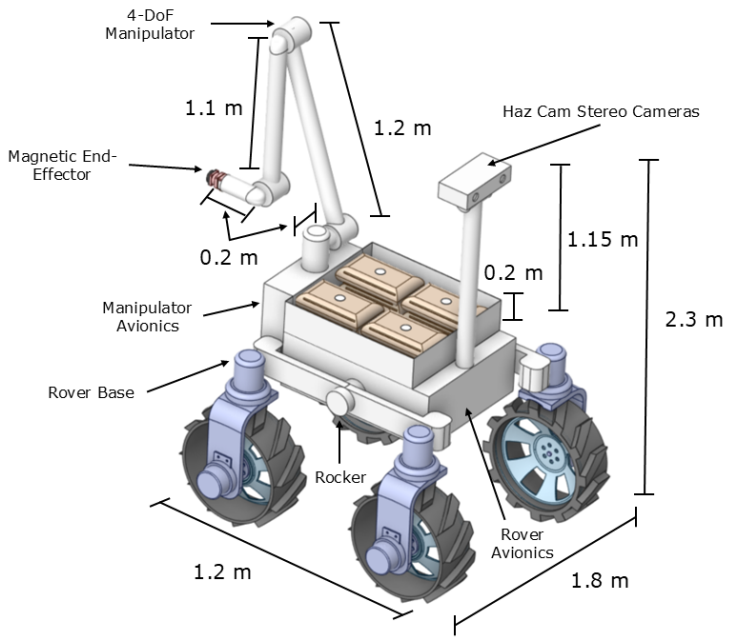

Figure 19. 3D Model Mobile Manipulator.

5.1. Mobility

The MM Mobility subsystem is designed according to GITAI's Lunar Rover [71]. This eliminates the need to further design the mobility base and ensures stability when operated with the 4-DoF manipulator, i.e., it does not tip over. Furthermore, it fits within the volumetric constraints and offers a simpler solution than alternatives such as ATHLETE [73–75]. The rover implements a 4-wheel dual-rocker suspension, reaching top speeds of 0.24 m/s. The wheels measure 0.6 m in diameter and are individually actuated by 4 brushless DC motors. All actuators implement dust-mitigation technologies. The rover also implements two Haz Cam stereo cameras [76] for navigation, mounted on a 1.15 m-tall mast. The processing is carried out by a Jetson Xavier onboard computer. The exact payload capacity of the rover is not specified; however, it can be seen from lunar analog demonstrations [77] that the rover can support at least 2 additional robotic systems and their payloads. The first of these robots is the Inchworm manipulator [78], with a mass of 50 kg and a payload capacity of 5 kg. The second robot is the S2 dual-arm manipulator, with a mass of at least 100 kg and a payload of at least 10 kg (estimated as two Inchworm manipulators). Furthermore, the base can carry an additional 20–40 kg of payload. This results in a total payload capacity of at least 200 kg for the rover mobility base. Overall, the system components have reached Technological Readiness Level (TRL) of 7 as of 2023.

The LRCS Mobility subsystem will need to stockpile RCUs in order to be able to place more than one RCU at a time in the blast berm. Considering the payload capacity of 200 kg, at least 8 RCUs, leaving some margin, could be transported per trip from the RB to the berm. Several RCU arrangement configurations can be considered for the stockpile, and three basic ones are shown in Figure 20. Configuration 1 is selected in this design since it allows for a higher manipulation error margin (more space between stacks) and all RCUs are in the same orientation, which simplifies the manipulation task. The stack of RCUs requires walls of 0.2 m to keep the RCUs secure, as shown in Figure 19.

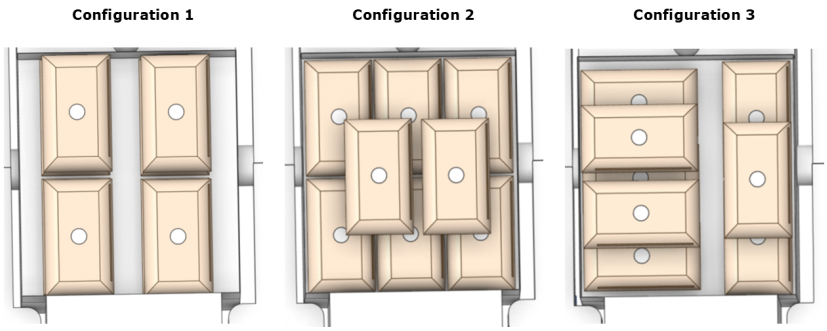

Figure 20. RCU Stockpiling Configurations.

5.2. RCU Manipulation

The RCU Manipulation subsystem consists of two primary physical pieces: the RCU manipulation interface and the articulated 4-DoF manipulator. The RCU manipulation interface refers to the magnetic end-effector on the 4-DoF manipulator, as well as the receiver on the RCU itself. The 4-DoF manipulator is mounted on the MM (see Section 5.1), and takes inspiration from COLDArm [70].

5.2.1. RCU Manipulation Interface

The LRCS Manipulator implements a magnetic end-effector to grasp the RCUs. The required attachment force for the end-effector per RCU is 22 kg $\times$ 1.625 m/s^2 = 35.75 N, which turns into 71.5 N with a safety factor of 2, in order to account for inefficiencies, e.g.,

dust on the interface. Generally, to select an appropriate electromagnet and contact area, one can consider the magnetic force formula

$$F_{magnetic} = \frac{B^2 \times A}{2\mu_0} \geq 71.5\ N, \tag{24}$$

where B is the magnetic flux, A is the contact surface area, and μ_0 is the permeability of free space. In practice, electromagnetic gripper manufacturers quantify these attachment forces for their electromagnet products. For example, the HGE-SQ-052-FR-EP-P-I electromagnetic gripper from Goudsmit Magnetics would match the requirements, with a working payload of 140 N, contact area of 0.0057 m diameter, and mass of 1 kg [79]. This already includes a safety factor of 3, enhancing redundancy. Furthermore, Goudsmit Magnetics has also quantified the thickness of low-carbon steel required to produce these attachment forces with varying air gaps, requiring 0.003 m-thick steel to produce 100 N of magnetic force at a 0.0001 m air gap [80]. These low-carbon steel interfaces could be woven into the fabric of the RCUs, and the distribution of the attachment force across the RCU surface should be investigated to prevent tearing. Additionally, the surface area of the steel could be expanded beyond the 0.0057 m diameter to add tolerance during interfacing. For the lack of space-grade electromagnetic grippers, an industrial gripper can be selected in the design, but it would need to be retrofitted for the lunar environment.

5.2.2. 4-DoF Manipulator

According to the requirements defined in Table A1, the 4-DoF Manipulator will need to reach a workspace volume of 2 m (depth) × 2.6 m (height) × 2 m (width), which aligns with the dimensions of the rover bed, discussed in Section 5.1. The two candidates articulated 4-DoF lunar manipulators are MDA Skymaker [81], with a maximum reach of 2.5 m, and COLDArm [70], with a maximum reach of 2 m. Considering that the Manipulator should be mounted on a rover bed of approximately 1 m high (see Section 5.1), both manipulators could reach the desired workspace. The end-effector payload capacities for Skymaker and COLDArm are 57 N and 40 N, respectively. Given the payload of 35.75 N per RCU (see Section 4.1), both Skymaker and COLDArm can effectively handle the payload. However, Skymaker is selected for the MM due to the larger workspace reach and payload capacity. Furthermore, similar to COLDArm, Skymaker is designed for the lunar environment, including the mitigation of lunar dust, temperature variations, and other environmental factors. The Skymaker manipulator link and joint parameters are presented in Table 7. An illustration of the reachable workspace for Skymaker, relative to the desired workspace, is shown in Figure 21, illustrating that it can comfortably cover the desired workspace. Table 8 lists Skymaker's operation time estimation. Given a 4°/s tip speed within the workspace, the average RCU placement speed from within the rover bed to a target 2 m away is 83.75 s.

Table 7. Link and Joint Parameters for Skymaker.

	Parameter	**Skymaker**
Joint Configuration	Total DOF	4
	Joint 1—Shoulder (Z-axis)	0° to 360°
	Joint 2—Shoulder (Y-axis)	−180° to +180°
	Joint 3—Elbow (Y-axis)	−180° to +180°
	Joint 4—Wrist (Y-axis)	−180° to +180°

Table 7. *Cont.*

	Parameter	Skymaker
Link Dimensions	Total Reach	2.5 m
	Link 1—Base to Shoulder	0.20 m
	Link 2—Upper Arm	1.2 m
	Link 3—Forearm	1.1 m
	Link 4—Wrist Section	0.20 m

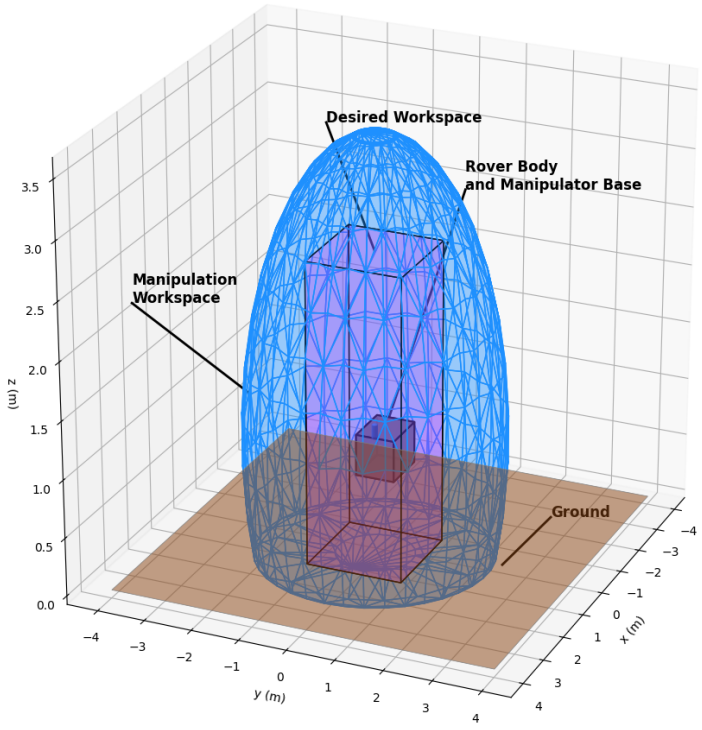

Figure 21. Skymaker Workspace versus Desired Workspace.

Table 8. LRCS RCU Placement Time Estimation.

Step	Operation	Time (s)
Step 1	Shoulder (z-axis) joint rotates 90°	22.5
Step 2	Shoulder/Elbow/Wrist (y-axis) joint rotates 45°	11.25
Step 3	Magnet engages RCU	1
Step 4	Shoulder/Elbow/Wrist (y-axis) joint rotates 45°	11.25
Step 5	Shoulder (z-axis) joint rotates 90°	22.5
Step 6	Shoulder/Elbow/Wrist joint (y-axis) rotates 45°	11.25
Step 7	Fine placement (y and z axes)	3
Step 8	Magnet disengages RCU	1
	Total Time	**83.75 s**

6. LRCS System Engineering: Common Subsystems

The RCU Bagger and the Mobile Manipulator also share some common subsystems, shown in Figure 22, namely Onboard Computing (Section 6.1), Power Management (Section 6.2), Communications (Section 6.3), Thermal Management (Section 6.4), and Lunar Dust Mitigation (Section 6.5). Since the MM is largely based on the Skymaker and GITAI Lunar Rover reference designs, the majority of the subsystem development is focused on the RB.

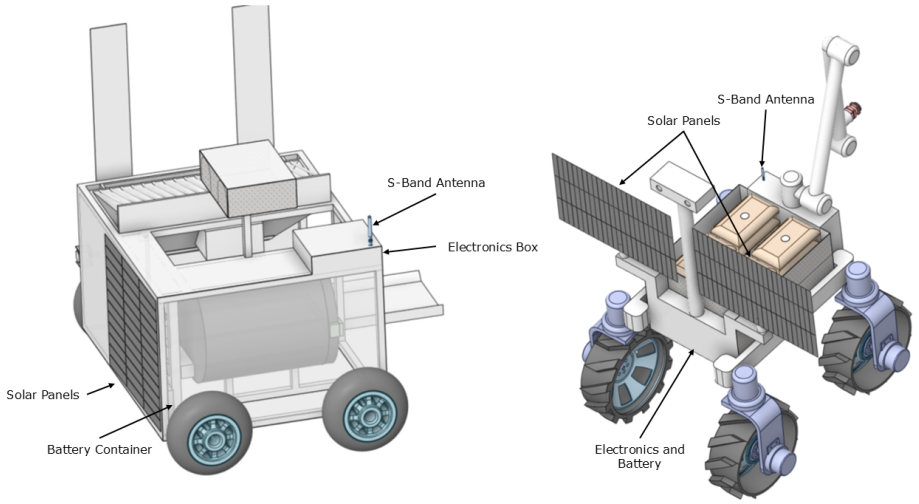

Figure 22. Common Subsystems for RB (**left**) and MM (**right**).

6.1. Onboard Computing

The LRCS onboard computer is generally required to manage command and control of the system, including performing global and local task planning, processing and fusing sensor data, driving the actuators, processing incoming and outgoing communications, and organizing memory resources. These functions, which are needed for both the RB and the MM, require a highly capable processor. In this design, the Jetson Xavier computer [82] is selected for both machines, inspired by GITAI's lunar rover [71]. This computing platform enables the implementation of advanced real-time vision systems, as well as high processing speeds to manage the variety of sensors and actuators simultaneously. The Jetson Xavier development kit has the complete electronics on a 1.68 kg printed circuit board, including 32 GB of storage, in a 0.105 m $\times$ 0.105 m $\times$ 0.065 m form factor [83].

The motor controller for the RB actuators is the same as the one for the COLDArm, which is a Dual-Axis Controller for Extreme Environments (DACEE), capable of controlling two motors at a time [70]. The controller design is based on the Bravo dual-axis motor controller from Motiv Space Systems [84]. Considering the bagging process in Figure 13 and the RB's differential steering (see Section 5.1), it is expected that four motors be active at any one time, requiring two DACEEs. Furthermore, the onboard computer will process thermal input data from thermistors and output commands to the thermal actuators. A high-level overview of the RB data flow is shown in Figure 23.

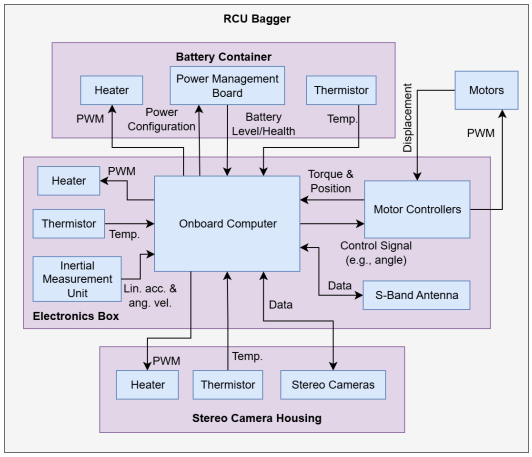

Figure 23. Data Flow for the RB Onboard Computer.

6.2. Power Management

For power generation, solar power concepts seek to leverage the near-constant illumination conditions of the lunar South Pole. These concepts find that solar arrays gain a mass advantage over nuclear reactors at polar sites illuminated for over 75% of a lunar cycle [85]. The state-of-the-art solar cells have energy densities up to 350 W/kg [86], as compared to 5 W/kg provided by the latest space-rated nuclear reactors, such as NASA's KRUSTY kilopower reactor [87]. Therefore, solar power is considered for the LRCS power generation. Both the RB and the MM will require solar panels; however, the MM will also require an actuator to rotate the panels towards the Sun. Since lunar dust will be a primary environmental factor, all solar panels should implement dust-mitigation technologies, such as the Electrodynamic Dust Shield (EDS) [88–90] (see Section 6.5), for dust clearing.

The LRCS also needs to store power throughout the duration of the mission scenario, accounting for variability in the solar power input and enabling the distribution of peak load power. Lithium-ion (Li-ion) batteries and Regenerative Fuel Cells (RFCs) are the primary technologies considered for long-duration energy storage on the lunar surface [85,91,92]. Although Li-ion batteries have a higher TRL, their specific energy level is typically around 200 Wh/kg [93], lower than the 300 to 1000 Wh/kg provided by RFCs [91,94]. It has been found that Li-ion batteries perform better for short discharge durations, while RFCs require lower mass for discharge durations over 10–18 h, such as the lunar night [92,95]. Considering that the LRCS mission scenario should be completed within a single lunar day, thus requiring shorter discharge durations, it is reasonable to select Li-ion batteries for power storage.

The power storage and generation architecture consists of some combination of Li-ion batteries and solar power. To evaluate the specific configuration and size of these components, a system-level power budget is developed in Section 7.1. A high-level power distribution architecture is presented for the RB in Figure 24 and for the MM in Figure 25. For both the RB and the MM, the solar panels act as the primary power source, supporting average system loads for the entirety of the mission scenario. The batteries act as a buffer for the system, giving a stable power source for the system to draw upon and allowing for up to 1 min of peak loading. The primary power rails for the RB include one high-voltage 28 DC voltage rail for the motors and one low-voltage 15 DC voltage rail for other electronics, such as the onboard computer. The power distribution for the MM is abstracted in Figure 25, since the power systems for the GITAI lunar rover and Skymaker manipulator are managed independently.

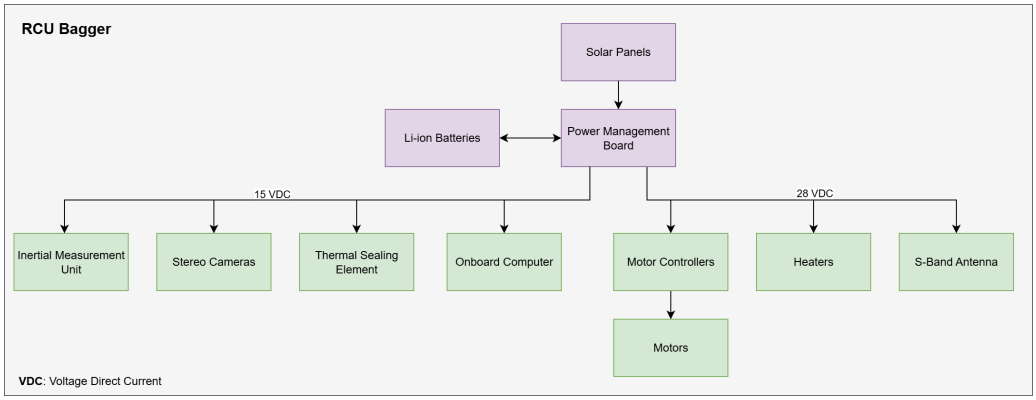

Figure 24. RB Power Distribution Architecture.

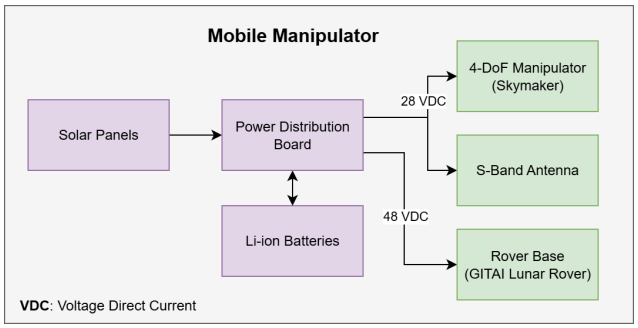

Figure 25. MM Power Distribution Architecture.

6.3. Communications

According to a NASA study, lunar communications terminals, such as the RB, can leverage the K/Ka band when communicating with Earth, as well as with lunar surface rovers, such as the MM [96]. The study anticipates that unmanned surface systems will require an estimated 10–25 Mbps throughput bandwidth. However, no existing systems currently meet this requirement. Current systems, such as India's Chandrayaan 3 and ESA's Pathfinder, communicate with Earth using the X-band [97,98]. Realistic mission scenarios will likely need to include relay satellites, such as ESA's Moonlight program [99]. In the absence of established lunar relay satellites, current mission scenarios typically leverage their lunar landers as communication relays [100], mitigating the need for a large communications array. One NASA study anticipates minimum X-band data rates of 17.1 Mbps for uplink and 1.9 Mbps for downlink from lunar relay satellites, as well as 2.17 Mbps for uplink and 2.31 Mbps for downlink from the lunar surface [101]. The Carnegie Mellon day-night lunar rover, a similar system to the LRCS, implements a 1 kg S-band antenna with 1 W of input power, achieving a 6 Mbps inter-rover communication data rate at a distance of up to 2 km [102]. This is used as the closest estimate for the LRCS Communications subsystem, assuming some lander (or orbital) relay, without fully designing a custom antenna and dish based on anticipated downlink/uplink data rates. The communications data flow for the LRCS is shown in Figure 26.

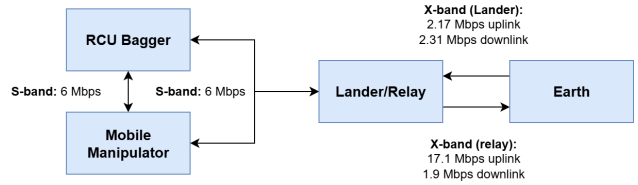

Figure 26. LRCS Communications Flow.

6.4. Thermal Management

The lunar South Pole experiences a wide range of surface temperatures. Diviner data collected over 10 years from the Lunar Reconnaissance Orbiter are used to make a comprehensive mapping of lunar surface temperatures [39], indicating that the temperature range and distribution for the lunar South Pole vary slightly throughout seasons, owing to the Moon's lack of weather and low axial tilt. However, there are slight increases in the size of cold spots during the winter. Generally, temperatures vary from over 300 K in the hottest regions to below 60 K in the coldest regions, the latter typically coinciding with PSRs in the craters.

The large temperature variation in the lunar South Pole poses challenges for surface systems such as the LRCS, for both material selection and electronics. For the LRCS thermal management, it is imperative to identify the components that require tight thermal control. The usage of the COLDArm motors and motor controllers, which are designed for the

lunar temperature range between 93 K and 373 K, dramatically reduces the complexity of the thermal management task [70]. Since the GITAI mobility base and Skymaker are both designed for the lunar surface, it is assumed that the thermal management for the MM is already considered for these systems. For the RB, the thermal management task can be further simplified by keeping the most sensitive electronic components grouped in a few locations. As such, only three locations within the RB may require active thermal management if passive thermal management is not sufficient. The first location is the battery container, which houses the power management board and the Li-ion batteries. The second location is the electronics box, which contains the onboard computer (see Section 6.1) and the S-band antenna (see Section 6.3), with related electronics, e.g., transceivers. The third location is the stereo camera housing. These three locations can be monitored using thermistors and thermally actuated using electronic heaters (see Figure 23). Small Kapton film heaters can be used to heat relevant components [103,104]. Lastly, it is assumed that the electronics of the system can be thermally coupled to the chassis for heat dissipation, eliminating the need for radiators. Furthermore, some components, such as the onboard computer, already have heat dissipation built in. However, further analysis is required in the follow-up stages of design to determine whether heaters, insulation, and radiators are necessary to maintain operable temperature ranges.

6.5. Lunar Dust Mitigation

The lunar dust has been documented as being highly abrasive and adhesive, as well as electrostatically charged [25]. This poses a challenging environmental factor for machinery, such as the LRCS, necessitating the implementation of mitigation technologies. To protect the solar panels, the Electrodynamic Dust Shield (EDS) can be employed, which is a high-TRL active dust mitigation technology, leveraging the electrostatic charging of lunar regolith to keep surfaces clear from dust [88–90,105–108]. Active methods, such as the EDS, will need to be combined with passive dust mitigation techniques. These techniques include surface coatings that minimize the dust attraction, such as the lotus leaf coating [48,109,110] and topology modification [48,111,112]. It is recommended that every dust-exposed surface of the LRCS be textured using a combination of these techniques, with the specific implementation depending on the final design and material selection. Furthermore, it is imperative that dust ingress to critical rotary interfaces be minimized, which can be achieved by implementing rotary dust seals, such as the spring-loaded Teflon seal [48,113,114]. Mature dust mitigation technologies for other interfaces are yet to be developed. One such challenging interface is the sealing of dust from prismatic movement interfaces, such as for lead-screw mechanisms. This could be achieved by modifying dust brushing mechanisms, such as the Zephyr fiberglass brush, to seal and clear dust from the interface [49].

6.6. Regolith Containment Unit

The detailed design of the RCUs is not performed in this work. The RCUs can be formed using Beta Cloth from Bron Aerotech, a material used in other space applications [115]. One trade study finds that Beta Cloth performs best as a barrier material for lunar regolith [48]. Some properties of Beta Cloth are summarized in Table 9. Of particular importance is the melting point of the material at 934 K. Given that Nichrome heating elements can operate up to 1673 K [64], Beta Cloth RCUs can be feasibly heat-sealed without the addition of a melting strip. Furthermore, the density of Beta Cloth is 1300 kg/m^3, lower than that of Kevlar (1440 kg/m^3), which is used as an analog in this work. Consequently, using Beta Cloth would reduce the estimated total system mass. However, future work

should perform a thorough analysis of Beta Cloth as the RCU material, including studying the specifics of the heat-sealing process and failure modes.

Table 9. Beta Cloth Properties (Courtesy: Bron Aerotech).

Substrate	Beta Fiberglass
Coating	PTFE
Weight	1300 kg/m^3
Thickness	0.0002 m
Breaking Strength (Warp)	2679 kg/m
Breaking Strength (Fill)	3036 kg/m
Melting Point	923 K

7. System Budgeting

7.1. Power Budgeting

To perform power budgeting for the LRCS, it is necessary to define the modes of operation of the system, which are broken down as follows:

LRCS Modes of Operation

- **Filling**—The RB intakes lunar regolith, deploys the empty RCU, fills the RCU, and seals the RCU.
- **Transfer**—The RB pushes the RCU out of the machine to be collected by the MM.
- **Manipulation**—The MM manipulates the RCU from the initial pose to the desired pose in the environment.
- **Idle**—The RB and/or MM remains in a live but inactive state; communications are still active.
- **Traversal**—The RB or MM traverses between various lunar surface locations.

Considering these modes of operation, a system-level power budget is presented in Table 10, adopting a set of power margins defined by NASA Ames [116]. Accordingly, a 30% power margin is taken for system-level design. A key assumption is made in formulating the power budget with regard to the mass of the solar panels and Li-ion batteries. Considering the constraint of 810 kg for the total mass of the LRCS (see Table A1), the power consumption for the RB drive motors is initially estimated based on a combined mass of 78 kg for its solar panels and batteries, prior to budgeting. Since the power consumption of the MM drive motors is already specified by the GITAI Lunar Rover, no initial estimate of the mass of the MM solar panels and batteries is needed.

Since the entire mission scenario is expected to take place during the lunar day, solar power will be the primary source for the LRCS. The battery acts as a buffer to distribute the power to the system, enabling some power storage for temporary periods of shadow and supporting peak loads. Figure 27 shows the load of the system (P_{RB} and P_{MM}) for one round-trip placement cycle to deploy 8 RCUs. Therefore, the cycle should be repeated 81,760 RCUs/8 RCUs = 10,220 times to complete the berm (see Section 2). The amount of power generated by solar panels can be quantified as [91,117]

$$P_{\mathrm{solar}} = (1 - \chi_d) \times f_{\mathrm{sc}} \times \eta_{\mathrm{sc}} \times A \times \phi sin(\alpha + \beta) \tag{25}$$

where χ_d is the percentage of dust coverage, f_{sc} is the solar array fill factor, η_{sc} is the solar cell efficiency, A is the solar array area, α and β are the Sun and array inclination

angles, respectively, and ϕ is the solar flux. For the LRCS operation, we can assume $\chi_d = 0$, $f_{sc} = 0.89$ [117], $\eta_{sc} = 0.32$ [86], and $\alpha + \beta = 90.5°$ (see Figure 7). The solar flux on the lunar surface varies from $\phi = 1308.9\ \mathrm{W/m^2}$ to $\phi = 1425.7\ \mathrm{W/m^2}$ [118], and the lowest value is considered for a conservative power budgeting. To power the system entirely using solar energy, $(P_{RB})_{solar} = 108\,\mathrm{W}$ and $(P_{MM})_{solar} = 1004\,\mathrm{W}$. Solving Equation (25) for A using these values results in solar panels of area $A = 0.26\,\mathrm{m^2}$ for the RB and $A = 2.4\,\mathrm{m^2}$ for the MM. This corresponds to one 0.5 m × 0.5 m panel for the RB and two 1 m × 0.6 m panels for the MM. Considering a solar cell mass density of $0.32\ \mathrm{kg/m^2}$ [86], the total mass of the solar arrays will then become 0.08 kg for the RB and 0.8 kg for the MM. The size of these panels can be reduced by optimizing the power system balance with the battery, relying on stored power for the most power-hungry modes of operation, and recharging the battery during periods of lower load.

Table 10. Power Budget for LRCS.

Component	Power (W, Avg/Peak)	Idle	Fill	Transfer	Traverse	Manipulate	Source
RCU Bagger (RB)							
Power Distribution Unit	4/7	100%	100%	100%	100%	100%	MarsFast
Onboard Computer	10/30	100%	100%	100%	100%	100%	Jetson Xavier
K/Ka Band Antenna	1/2	20%	20%	20%	20%	20%	Carnegie Mellon
Vibratory Motor	0.36/56	0%	36%	0%	0%	0%	COLDArm
Linear Actuator (Funnel)	0.008/56	0%	5%	0%	0%	0%	COLDArm
Linear Actuator (Arm)	0.005/56	0%	3%	0%	0%	0%	COLDArm
Rotary Motor (Arm)	3.2/56	0%	89%	0%	0%	0%	COLDArm
Roller Motors (Arm ×2)	0.6/112	0%	80%	0%	0%	0%	COLDArm
Thermal Sealing Element	413/600	0%	7%	0%	0%	0%	Estimate
Roller Motor (Storage)	1/56	0%	11%	50%	0%	0%	COLDArm
Rotary Motor (Lever Arm)	1/56	0%	0%	100%	0%	0%	COLDArm
Rotary Motor (Ramp)	0.8/56	0%	0%	0%	1%	0%	COLDArm
Stereo Cameras (×2)	2/4	0%	20%	20%	100%	0%	Mastcam-Z
Inertial Measurement Unit	0.4/0.8	0%	0%	0%	100%	0%	MarsFast
Mast Motors (×2)	0.26/112	0%	20%	20%	100%	0%	COLDArm
Drive Motors (×4)	26/224	0%	0%	0%	100%	0%	COLDArm
Motor Controllers (×2)	5/10	0%	100%	100%	100%	0%	DACEE (COLDArm)
Heater (Electronics Box)	5/10	100%	100%	100%	100%	100%	OMEGA
Heater (Stereo Cameras)	5/10	100%	100%	100%	100%	100%	OMEGA
Heater (Battery)	20/40	100%	100%	100%	100%	100%	OMEGA
RB Total Load (W)	–	44/97	82/343	51/215	78/449	44/97	–
RB Total Load with Margin (W)	–	57/127	107/446	66/279	101/583	57/127	–
Mobile Manipulator (MM)							
K/Ka Band Antenna	1/2	20%	20%	20%	20%	20%	Carnegie Mellon
Rover Base (incl. avionics)	750/1500	10%	10%	10%	100%	10%	GITAI
4-DoF Manipulator (incl. avionics)	220/310	10%	10%	10%	10%	100%	Skymaker
Electromagnet	4.8/120	0%	0%	0%	0%	100%	Goudsmit Magnetics
MM Total Load (W)	–	97/181	97/181	97/181	772/1531	300/580	–
MM Total Load with Margin (W)	–	126/236	126/236	126/236	1004/1991	390/755	–
LRCS Total Load (W)	–	141/279	180/524	148/396	850/1980	344/678	–
LRCS Total Load with Margin (W)	–	184/362	235/682	193/515	1105/2574	447/881	–

The battery properties can be determined by considering the peak loads of the system from Table 10. To support one minute of peak load for the RB and the MM, where $(P_{RB})_{peak} = 583\,\mathrm{W}$ and $(P_{MM})_{peak} = 1991\,\mathrm{W}$, the system batteries need to contain

$$E_{\text{battery RB}} = P_{\text{peak RB}} \times t_{\text{peak}} = 583\,\mathrm{W} \times 60\,\mathrm{s} = 34980\,\mathrm{J} \quad (26)$$

$$E_{\text{battery MM}} = P_{\text{peak MM}} \times t_{\text{peak}} = 1991\,\mathrm{W} \times 60\,\mathrm{s} = 119460\,\mathrm{J} \quad (27)$$

of energy capacity. Accounting for a battery charging efficiency of $\eta_{\text{charging}} = 0.99$ [91] and an allowable depth of discharge (DoD) of 40% [116], the desired battery capacity (C) can be found as

$$C_{RB} = \frac{E_{\text{battery RB}}}{\text{DoD} \times \eta_{\text{charging}}} = \frac{34980\,\text{J}}{0.4 \times 0.99} = 88333\,\text{J} = 24.5\,\text{Wh} \tag{28}$$

$$C_{MM} = \frac{E_{\text{battery MM}}}{\text{DoD} \times \eta_{\text{charging}}} = \frac{119460\,\text{J}}{0.4 \times 0.99} = 301667\,\text{J} = 83.8\,\text{Wh}\,. \tag{29}$$

Using a Li-ion energy density of $\rho_{\text{li-ion}}$ = 200 Wh/kg or 720,000 J/kg, the total battery mass for the RB and MM can be calculated as

$$m_{\text{battery RB}} = \frac{C_{RB}}{\rho_{\text{li-ion}}} = \frac{88333\,\text{J}}{720000\,\text{J/kg}} = 0.12\,\text{kg} \tag{30}$$

$$m_{\text{battery MM}} = \frac{C_{MM}}{\rho_{\text{li-ion}}} = \frac{301667\,\text{J}}{720000\,\text{J/kg}} = 0.42\,\text{kg}\,. \tag{31}$$

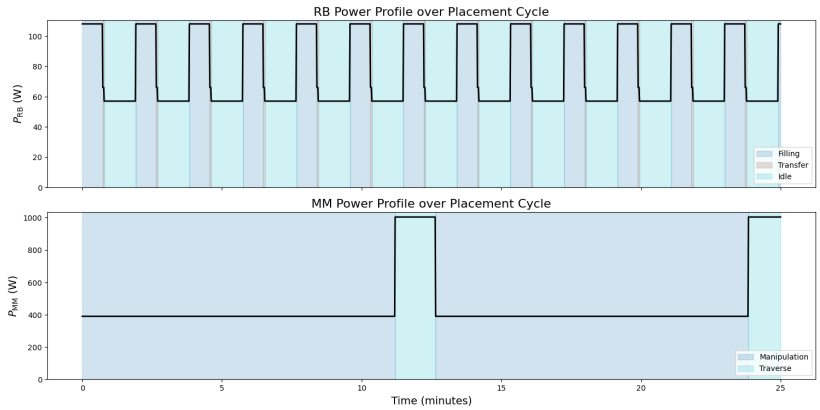

Figure 27. LRCS Power Consumption Over One Placement Cycle.

7.2. Mass Budgeting

The mass budgeting of the LRCS is detailed in Table 11. The American Institute of Aeronautics and Astronautics (AIAA) recommends a set of mass margins and mass growth allowances (MGA) [119], which are adopted in this work. Component masses are taken from the aforementioned reference designs, such as COLDArm for the actuators or Skymaker for the 4-DoF Manipulator. Additional reference designs include MarsFast [120] for some common system components, such as the power distribution unit, and Carnegie Mellon's lunar rover [102] for the S-band antenna.

Table 11. System-level Mass Budget with Subsystem Breakdown.

Subsystem	Component	RB/MM	Maturity	MGA (%)	Mass (kg)	Mass + MGA (kg)	Source
Structural					**31.68**	**34.85**	
	Chassis	RB	E2	10%	14.40	15.84	Model
	Plating	RB	E2	10%	10.27	11.30	Model
	Ramp	RB	E2	10%	1.96	2.16	Model
	Motor (Ramp)	RB	E2	10%	1.40	1.54	COLDArm
	RCU Stockpile Storage	MM	E2	10%	3.65	4.02	Model
Thermal					**0.27**	**0.31**	
	3 × Heater	RB	E2	15%	0.02	0.02	OMEGA
	Insulation	RB	E2	15%	0.25	0.29	MarsFast

Table 11. *Cont.*

Subsystem	Component	RB/MM	Maturity	MGA (%)	Mass (kg)	Mass + MGA (kg)	Source
Power Management					**18.42**	**22.06**	
	Solar Panels	RB	E2	10%	0.08	0.09	Section 7.1
	Solar Panels	MM	E2	10%	0.80	0.88	Section 7.1
	Li-Ion Batteries	RB	E2	10%	0.12	0.13	Section 7.1
	Li-Ion Batteries	MM	E2	10%	0.42	0.46	Section 7.1
	Power Distribution Unit	RB	E2	15%	7.00	8.05	MarsFast
	Cabling	RB	E2	20%	10.00	12.00	Carnegie Mellon
Communications					**2.00**	**2.30**	
	S-Band Antenna	RB	E2	15%	1.00	1.15	Carnegie Mellon
	S-Band Antenna	MM	E2	15%	1.00	1.15	Carnegie Mellon
Onboard Computing					**2.05**	**2.37**	
	CPU and Memory	RB	E2	15%	0.84	0.97	Jetson Xavier
	CPU and Memory	MM	E2	15%	0.84	0.97	Jetson Xavier
	2 × Motor Controller	RB	E2	15%	0.37	0.43	DACEE (COLDArm)
Filling					**104.51**	**114.09**	
	4 × Rollers	RB	E2	10%	1.76	1.94	Model
	Storage Cylinder	RB	E2	10%	4.78	5.26	Model
	RCU Roll	RB	E2	10%	77.80	85.58	Model
	1-DoF Arm	RB	E2	10%	0.36	0.40	Model
	Vibrating Funnel	RB	E2	10%	8.10	8.91	Model
	Sliding Door	RB	E2	10%	1.54	1.69	Model
	Vibratory Motor	RB	E2	15%	1.40	1.61	COLDArm
	2 × Linear Actuator	RB	E2	15%	2.80	3.22	COLDArm
	4 × Motor	RB	E2	15%	5.60	6.44	COLDArm
	Gearbox	RB	E2	10%	0.37	0.41	Model
Transfer					**6.08**	**6.76**	
	Chute	RB	E2	10%	4.32	4.75	Model
	Lever Arm	RB	E2	10%	0.36	0.40	Model
	DC Brushless Motor	RB	E2	15%	1.40	1.61	COLDArm
Manipulation					**41.00**	**43.15**	
	4-DoF Manipulator	MM	C3	5%	40.00	42.00	Skymaker
	Electromagnet	MM	E2	15%	1.00	1.15	Goudsmit Magnetics
Mobility					**299.54**	**325.50**	
	2 × Stereo Camera	RB	E2	15%	2.76	3.17	Mastcam-Z
	Inertial Measurement Unit	RB	E2	15%	0.30	0.35	MarsFast
	2 × Motor (Mast)	RB	E2	15%	2.80	3.22	COLDArm
	4 × Wheels	RB	E2	10%	8.08	8.89	LRV Wheels
	4 × Motor	RB	E2	10%	5.60	6.16	COLDArm
	4-Wheel Rover	MM	C3	5%	280.00	294.00	GITAI
RCU Bagger					**177.84**	**197.98**	
Mobile Manipulator					**327.71**	**344.63**	
Total					**505.55**	**542.61**	

7.3. Cost Budgeting

A preliminary cost budgeting for the LRCS is performed by applying the Advanced Mission Cost Model (AMCM) [121]. The AMCM considers the system mass, launch year (2030), difficulty, and maturity [122]. The maturity of the system is based on the Block Number, representing the level of design inheritance, e.g., two or more for a second-generation design onward. These factors vary between the RB and the MM; therefore, they are considered separately in Table 12. The AMCM finds an anticipated cost of 631 million USD for RB and 709 million USD for the MM. The estimated total cost, including a 30% margin, would end up to 1742 million USD. The estimated costs are particularly influenced by the programmatic and technical difficulty that are foreseen for the system and the task it is expected to perform. Since both the RB and the MM machines are new complex systems, the level of difficulty adopted for the system is selected as "very high."

Table 12. Illustrative AMCM Parameter Breakdown for LRCS Elements.

System	Mass [kg]	Difficulty	Block No.	Cost Estimate [Million USD]
RB	197.98	Very High	1	631
MM	344.63	Very High	2	709
LRCS Total				**1340**
LRCS Total with Margin *				**1742**

* Total with 30% margin applied.

8. Conclusions

A Lunar Robotic Construction System (LRCS) was detail-designed. The system is intended to utilize raw lunar regolith for constructing surface structures through the bagging and manipulation of Regolith Containment Units (RCUs). The work is motivated by the need for scalable construction systems capable of building protective berms, as well as other infrastructure, where reliance on in situ resources will be critical to sustainable surface operations. The RCUs require minimal regolith processing, making them ideal candidates for building simple structures, as well as providing physical, radiation, and thermal protection.

The LRCS consists of two machines, the RCU Bagger (RB), which fills and seals the RCUs, and the Mobile Manipulator (MM), which transports and places the RCUs in the desired locations. The construction of a blast berm for a lunar landing pad was investigated as a mission scenario for the LRCS. While the RB is a largely novel machine, the MM takes inspiration from the GITAI Lunar Rover and Skymaker manipulator reference designs. Continuing the work of the LRCS conceptualization [20], this paper presented the subsystem design for the LRCS, focusing on the primary subsystems, namely RCU Filling, RCU Transfer, RCU Manipulation, and Mobility. The high-level design for the other common subsystems was also discussed. The initial analyses of the RB and MM indicate the feasibility of the LRCS concept. A structural analysis of the RB chassis was performed, as well as simulations of the regolith intake mechanism. Operational analyses indicate that berm construction is feasible for the LRCS when deployed with a swarm of 6 or more IPEx systems. Initial estimations of mass, power, and cost were obtained for the LRCS.

Future studies should extend the work through more detailed subsystem engineering, physical prototyping, and laboratory experiments with high-fidelity regolith simulants, particularly in order to validate intake, filling, and stacking mechanisms under lunar-representative conditions. Further work should be done to develop the RCU building block, including testing of the theorized protective properties (physical, thermal, and radiative). Simulation studies should also be extended to creating more realistic lunar regolith and RCU modeling. The integration of autonomy, perception, and dust-mitigation technologies will also be critical to achieving scalable and reliable operations. Expanding the scope of construction tasks beyond berm formation to include landing pad foundations, radiation shielding, and modular habitat walls would further demonstrate the validity and versatility of the LRCS. Further studies can also consider the deployment of multiple RBs or MMs depending on operational requirements. Moreover, on a larger scale, the impact of resource extraction (regolith) should be investigated to analyze the sustainability of construction activities on the lunar surface.

Author Contributions: Conceptualization, K.V. and M.R.E.; Methodology, M.R.E.; Software, K.V.; Validation, K.V. and M.R.E.; Formal analysis, K.V. and M.R.E.; Investigation, K.V. and M.R.E.; Resources, M.R.E.; Data curation, K.V.; Writing—original draft, K.V.; Writing—review and editing,

M.R.E.; Visualization, K.V.; Supervision, M.R.E.; Project administration, M.R.E.; Funding acquisition, M.R.E. All authors have read and agreed to the published version of the manuscript.

Funding: This research received funding from MDA Space Ltd. and the University of Toronto.

Data Availability Statement: The original contributions presented in this study are included in the article. Further inquiries can be directed to the corresponding author. Data available in a publicly accessible repository. The original data presented in the study are openly available on GitHub at https://github.com/natek1234/automatic_AHP_and_ZM_2 (accessed on 8 October 2025).

Acknowledgments: The authors would like to acknowledge the financial and in-kind support provided by MDA Space Ltd. In particular, we would like to thank Cameron Dickinson for his insightful comments and suggestions throughout the conceptualization process. The in-kind provisions of the University of Toronto for this work are also acknowledged.

Conflicts of Interest: Author Ketan Vasudeva was employed by the company MDA Space Ltd. The remaining authors declare that the research was conducted in the absence of any commercial or financial relationships that could be construed as a potential conflict of interest.

Appendix A. System Requirements

Table A1. System Requirements [20] (with some modifications).

ID	Requirement: The System Shall ...
	Functional Requirements
SYS-F-01	intake lunar regolith from an external lunar regolith excavation and processing system.
SYS-F-02	beneficiate lunar regolith.
SYS-F-03	transfer excess regolith to a third-party Regolith and Analysis Processing Subsystem.
SYS-F-04	fill the RCUs with lunar regolith.
SYS-F-05	seal the RCUs.
SYS-F-06	internally transfer the RCUs from the filling configuration to the manipulation configuration.
SYS-F-07	be decoupled into a mobile manipulation system and a centralized RCU filling system.
SYS-F-08	interface with and secure the RCUs for manipulation.
SYS-F-09	manipulate the RCUs into a desired pose within the environment.
SYS-F-10	be able to move and localize itself in the lunar environment.
SYS-F-11	have onboard computing capabilities.
SYS-F-12	collect and store system health and history data.
SYS-F-13	be able to communicate with the lunar surface and orbital communication systems.
SYS-F-14	generate, store, and manage sufficient power for operation during the operational lifetime.
SYS-F-15	be able to maintain its thermal state within operable ranges.
SYS-F-16	be capable of operating in the lunar environment.
SYS-F-17	be deployable from a launch vehicle to the lunar surface.
	Performance Requirements
SYS-P-01	support a sustained operational (average) power draw of at least 1100 W (see Section 7.1, modified from [20]).
SYS-P-02	support a peak operational power draw of at least 2600 W for 1 min (see Section 7.1, modified from [20]).
SYS-P-03	be capable of filling and sealing 1 RCU in under 2.7 min (see Section 2, modified from [20]).
SYS-P-04	be capable of manipulating an average of 1 RCU into the berm in under 163 s (see Section 2).
SYS-P-05	have an operational lifetime of 6 months (see Section 2).
SYS-P-06	have a total battery charge of at least 110 Wh (see Section 7.1, modified from [20]).
SYS-P-07	be capable of reaching a manipulation workspace volume of 2 m $\times$ 2.6 m $\times$ 2 m (depth, height, width).
SYS-P-08	be capable of reaching a mobility workspace area of $\pi \times (50\text{m})^2 = 2500\ \text{m}^2$.
SYS-P-09	be capable of intaking at least 60 kg of lunar regolith (double IPEx capacity).
SYS-P-10	be capable of bagging and stacking 81,760 RCUs (see Section 2, in addition to [20]).
SYS-P-11	be capable of repeatably stacking 4 RCUs vertically 20,440 times (see Section 2, in addition to [20]).

Table A1. *Cont.*

ID	Requirement: The System Shall ...
	Environmental Requirements
SYS-E-01	have an operational temperature range of 60 K to 190 K [123].
SYS-E-02	have a survivable temperature range of 40 K to 230 K [123].
SYS-E-03	maintain the temperature of electronics between 233 K and 358 K.
SYS-E-04	be capable of withstanding a total radiation dose of at least 0.5 Sv.
SYS-E-05	operate while exposed to a maximum solar irradiance of 1425.7 W/m^2 [118].
SYS-E-06	operate while exposed to lunar regolith and lunar regolith dust [124].
SYS-E-07	operate in an ambient pressure of 3×10^{-15} atm [125].
	Constraints
SYS-C-01	have a maximum mass of 810 kg (for medium-class lander).
SYS-C-02	have a maximum stowed volume of 6 m^3.
SYS-C-03	use non-rigid RCUs with dimensions of 0.43 m $\times$ 0.25 m $\times$ 0.10 m.
SYS-C-04	use RCUs with a mass of 22 kg.
SYS-C-05	have a regolith intake interface of dimension 0.625 m $\times$ 0.312 m to accommodate IPEx.

References

1. Bennett, T.; Cain, C.; Campbell, N.; Gemer, A.J.; Green, T.; Niederweiser, T. Engineering the CisLunar Economic System based on ULA's CisLunar-1000 Vision. In Proceedings of the AIAA SPACE 2016, Long Beach, CA, USA, 13–16 September 2016; American Institute of Aeronautics and Astronautics: Reston, VA, USA, 2016. [CrossRef]
2. Chavy-Macdonald, M.A.; Oizumi, K.; Kneib, J.P.; Aoyama, K. The cis-lunar ecosystem—A systems model and scenarios of the resource industry and its impact. *Acta Astronaut.* **2021**, *188*, 545–558. [CrossRef]
3. Schmitt, H. Apollo 17 and the Moon. In *Encyclopedia of Space Science and Technology*; John Wiley & Sons, Ltd.: Hoboken, NJ, USA, 2003. [CrossRef]
4. Creech, S.; Guidi, J.; Elburn, D. Artemis: An overview of NASA's activities to return humans to the Moon. In *Proceedings of the 2022 IEEE Aerospace Conference*; IEEE: Piscataway, NJ, USA, 2022; pp. 1–7.
5. Häuplik-Meusburgera, S.; Messinab, P. Envisioning the Moon Village–A Space Architectural Approach. In Proceedings of the 69th International Astronautical Congress, Bremen, Germany, 1–5 October 2018.
6. Köpping Athanasopoulos, H. The Moon Village and Space 4.0: The 'Open Concept' as a New Way of Doing Space? *Space Policy* **2019**, *49*, 101323. [CrossRef]
7. Petrov, G.; Inocente, D.; Haney, M.; Katz, N.; Koop, C.; Makaya, A.; Arnhof, M.; Lakk, H.; Cowley, A.; Haignere, C.; et al. Moon village reference masterplan and habitat design. In Proceedings of the ICES. 49th International Conference on Environmental Systems, Boston, MA, USA, 7–11 July 2019.
8. ESA. *Moon Village: Conceptual Design of a Lunar Habitat*; CDF Study Report ESA-CDF-202(A); European Space Agency: Paris, France, 2020.
9. Xu, F.; Ou, J. Promoting international cooperation on the International Lunar Research Station: Inspiration from the ITER. *Acta Astronaut.* **2023**, *203*, 341–350. [CrossRef]
10. Jones, A. *Senegal Among New Members of China's ILRS Moon Base Project*; SpaceNews: Alexandria, VA, USA, 2024.
11. ISECG. *The Global Exploration Roadmap*; Technical Report. ISECG, 2024. Available online: https://www.globalspaceexploration.org/wp-content/isecg/GER2024.pdf (accessed on 19 May 2026).
12. Lane, J.E.; Metzger, P.T. Estimation of Apollo Lunar Dust Transport using Optical Extinction Measurements. *Acta Geophys.* **2015**, *63*, 568–599. [CrossRef]
13. Vasudeva, K.; Emami, M.R. Lunar Construction: A State-of-the-art Survey. *Prog. Aerosp. Sci.* **2026**, *161*, 101159. [CrossRef]
14. Bao, C.; Zhang, D.; Wang, Q.; Cui, Y.; Feng, P. Lunar In Situ Large-Scale Construction: Quantitative Evaluation of Regolith Solidification Techniques. *Engineering* **2024**, *39*, 204–221. [CrossRef]
15. Raj, A.T.; Qiu, J.; Vilvanathan, V.; Xu, Y.; Asphaug, E.; Thangavelautham, J. Systems Engineering of Using Sandbags for Site Preparation and Shelter Design for a Modular Lunar Base. In *Proceedings of the Earth and Space 2022*; American Society of Civil Engineers: Reston, VA, USA, 2023. [CrossRef]
16. Cannon, R.; Henninger, S.; Levandoski, M.; Perkins, J.; Pitchon, J.; Swats, R.; Wessels, R. *TEX 4312/ME 4182 NASA/USRA Advanced Design Program: Lunar Regolith Bagging System*; Technical Report; NASA: Washington DC, USA, 1990.
17. Brown, S.; Lundberg, K.; McGarity, G.; Silverman, P. *TEX 4312/ME 4182 NASA/USRA Advanced Design Program: Lunar Regolith Bagging System*; Technical Report; NASA: Washington DC, USA, 1990.
18. NASA. *A One-Piece Lunar Regolith Bag Garage Prototype*; Technical Report; NASA: Washington DC, USA, 2007.

19. Singh, M. Construction Technique and Strength of Connected Regolith Bag Structures. Ph.D. Thesis, Auburn University, Auburn, AL, USA, 2007.
20. Vasudeva, K.; Emami, M.R. Lunar Robotic Construction System Using Raw Regolith: Design Conceptualization. *Aerospace* **2025**, *12*, 947. [CrossRef]
21. Lane, J.E.; Metzger, P.T.; Immer, C.D.; Li, X. Lagrangian Trajectory Modeling of Lunar Dust Particles. In *Proceedings of the Earth & Space 2008*; American Society of Civil Engineers: Reston, VA, USA, 2008; pp. 1–9. [CrossRef]
22. Harada, T.; Usami, R.; Takadama, K.; Kamata, H.; Ozawa, S.; Fukuda, S.; Sawai, S. Computational Time Reduction of Evolutionary Spacecraft Location Estimation toward Smart Lander for Investigating Moon. In Proceedings of the 11th International Symposium on Artificial Intelligence, Robotics and Automation in Space (i-SAIRAS2012), Turin, Italy, 4–7 September 2012.
23. Anzalone, E.; Iyer, A.; Statham, T. Use of Navigation Beacons to Support Lunar Vehicle Operations. In *Proceedings of the 2020 IEEE Aerospace Conference*; IEEE: Piscataway, NJ, USA, 2020; pp. 1–13. [CrossRef]
24. Edwards, D.L.; Cooke, W.; Suggs, R.; Moser, D.E. *Analysis of Regolith Simulant Ejecta Distributions from Normal Incident Hypervelocity Impact*; Technical Report MSFC-828; NASA Marshall Space Flight Center: Huntsville, AL, USA, 2008.
25. Heiken, G.H.; Vaniman, D.T.; French, B.M. *Lunar Sourcebook: A User's Guide to the Moon*; Cambridge University Press: Cambridge, MA, USA, 1991.
26. Khalil, N. Simulation and Experimentation of Interactions and Robotic Manipulation of Regolith Containment Units for Lunar Construction. Bachelor's Thesis, University of Toronto, Toronto, ON, Canada, 2026.
27. Astrobotic. Landers. 2025. Available online: https://www.astrobotic.com/lunar-delivery/landers/ (accessed on 17 June 2025).
28. Blue Origin. Blue Moon Mark 1. 2025. Available online: https://www.blueorigin.com/blue-moon/mark-1 (accessed on 17 June 2025).
29. Firefly Space. Blue Ghost. 2025. Available online: https://fireflyspace.com/blue-ghost/ (accessed on 17 June 2025).
30. Intuitive Machines. Nova-C. 2025. Available online: https://www.intuitivemachines.com/nova-c (accessed on 17 June 2025).
31. Intuitive Machines. Nova-D. 2025. Available online: https://www.intuitivemachines.com/nova-d (accessed on 17 June 2025).
32. iSpace. APEX 1.0 Lunar Lander. 2025. Available online: https://ispace-us.com/mission-3/ (accessed on 17 June 2025).
33. European Space Agency. Argonaut: Europe's Lunar Lander Programme. 2025. Available online: https://www.esa.int/Science_Exploration/Human_and_Robotic_Exploration/Exploration/Argonaut_Europe_s_lunar_lander_programme (accessed on 17 June 2025).
34. Schuler, J.; Smith, J.D.; Nick, A.J.; Buckles, B.C.; Dyas, J.E.; Ortega, V.V.; Cloud, J.M.; Dokos, A.G.; Zhang, E.L.; Wang, J.J.; et al. ISRU Pilot Excavator (IPEx) Technology Readiness Level 5 Design Overview. In *Proceedings of the AIAA Aviation Forum and ASCEND 2024, Las Vegas, NV, USA, 29 July–2 August 2024*; American Institute of Aeronautics and Astronautics: Reston, VA, USA, 2024; p. 4890.
35. NASA. NASA Identifies Candidate Regions for Landing Next Americans on Moon. 2022. Available online: https://www.nasa.gov/news-release/nasa-identifies-candidate-regions-for-landing-next-americans-on-moon/#:~:text=%E2%80%9CWhen%20we%20do%2C%20it%20will,Peak%20Near%20Shackleton (accessed on 17 June 2024).
36. Hu, T.; Yang, Z.; Li, M.; van der Bogert, C.H.; Kang, Z.; Xu, X.; Hiesinger, H. Possible sites for a Chinese International Lunar Research Station in the Lunar South Polar Region. *Planet. Space Sci.* **2023**, *227*, 105623. [CrossRef]
37. USGS. MOON—Shackleton. 2023. Available online: https://planetarynames.wr.usgs.gov/Feature/5450 (accessed on 19 July 2025).
38. NASA. SPICE. 2025. Available online: https://naif.jpl.nasa.gov/naif/index.html (accessed on 19 July 2025).
39. Williams, J.P.; Greenhagen, B.T.; Paige, D.A.; Schorghofer, N.; Sefton-Nash, E.; Hayne, P.O.; Lucey, P.G.; Siegler, M.A.; Aye, K.M. Seasonal Polar Temperatures on the Moon. *J. Geophys. Res. Planets* **2019**, *124*, 2505–2521. [CrossRef]
40. Saaty, T.L.; Vargas, L.G. *Models, Methods, Concepts & Applications of the Analytic Hierarchy Process*; Springer: New York, NY, USA, 2012. [CrossRef]
41. Nisbett, J.K.; Budynas, R.G. *Shigley's Mechanical Engineering Design*; McGraw-Hill: New York, NY, USA, 2020.
42. NASA. *Structural Design and Test Factors of Safety for Spaceflight Hardware*; Technical Report NASA-STD-5001B; NASA: Washington DC, USA, 2016.
43. NASA. *Standard Materials and Processes Requirements for Spacecraft*; Technical Report NASA-STD-6016C; NASA: Washington DC, USA, 2023.
44. Kopec, M.; Liu, X.; Gorniewicz, D.; Modrzejewski, P.; Zasada, D.; Jóźwiak, S.; Janiszewski, J.; Kowalewski, Z.L. Mechanical response of 6061-T6 aluminium alloy subjected to dynamic testing at low temperature: Experiment and modelling. *Int. J. Impact Eng.* **2024**, *185*, 104843. [CrossRef]
45. Battelle Memorial Institute. *Metallic Materials Properties Development and Standardization (MMPDS-01)*; Federal Aviation Administration: Columbus, OH, USA, 2003.
46. McMaster-Carr. Multipurpose 6061 Aluminum Rectangular Tubes. 2025. Available online: https://www.mcmaster.com/products/aluminum-square-tubing/multipurpose-6061-aluminum-rectangular-tubes/ (accessed on 20 July 2025).

47. McMaster-Carr. Multipurpose 6061 Aluminum Sheets and Bars. 2025. Available online: https://www.mcmaster.com/products/aluminum-plates/multipurpose-6061-aluminum-sheets-and-bars-7/ (accessed on 20 July 2025).
48. Cannon, K.M.; Dreyer, C.B.; Sowers, G.F.; Schmit, J.; Nguyen, T.; Sanny, K.; Schertz, J. Working with lunar surface materials: Review and analysis of dust mitigation and regolith conveyance technologies. *Acta Astronaut.* **2022**, *196*, 259–274. [CrossRef]
49. Gaier, J.R.; Journey, K.; Christopher, S.; Davis, S. Evaluation of brushing as a lunar dust mitigation strategy for thermal control surfaces. In *Proceedings of the 41st International Conference on Environmental Systems*; NASA: Washington DC, USA, 2011; Number NASA/TM-2011-217231.
50. Inoue, D.; Yanagihara, Y.; Ueno, H.; Nishida, S. Model Tests of Regolith Packaging Mechanism. *J. Robot. Mechatron.* **2012**, *24*, 1023–1030. [CrossRef]
51. Tinsley. Types of Bagging Machines. 2024. Available online: https://www.tinsleycompany.com/types-of-bagging-machines/ (accessed on 10 December 2024).
52. TechnoPack. What are The Different Types of Bagging Machines? 2024. Available online: https://technopackcorp.com/blogs/news/what-are-the-different-types-of-bagging-machines?srsltid=AfmBOopGbpYsVH2mR5uC_ljg3s_ohIDtH8XMZgk77LfR1D-ap6ijJcUE (accessed on 10 December 2024).
53. Payper. Products. 2024. Available online: https://www.payperindia.com/bagging.html (accessed on 10 December 2024).
54. TMI. Bagging Systems. 2024. Available online: https://www.tmipal.com/en/solutions/bagging-systems (accessed on 10 December 2024).
55. LinkPack. A Guide to Automated Bagging Machines. 2024. Available online: https://link-pack.com/automated-bagging-machines-a-complete-guide/ (accessed on 10 December 2024).
56. Concetti. Industrial Bagging Machines: Explore Our Latest Solutions. 2024. Available online: https://www.concetti.com/en-us/news-and-events/129-news/1210-industrial-bagging-machines-explore-our-latest-solutions (accessed on 10 December 2024).
57. Inpak Systems Inc. Bag Filling & Weighing Equipment. 2024. Available online: https://www.inpaksystems.com/bag-filling/ (accessed on 10 December 2024).
58. Watson, P.; Bonnieu, S.V.; Anwar, A.; Lappa, M. Experimental analysis of vibrationally-induced fluidization of lunar regolith in hoppers and closed containers. In Proceedings of the 75th International Astronautical Congress, Milan, Italy, 14–18 October 2024.
59. Bendixen Noe, J.; van Susante, P.; Sibille, L.; Pinto-Reveggino, J. Static and Kinetic Friction Coefficients for Regolith Delivery into a Molten Regolith Electrolysis Reactor. In *Proceedings of the Earth and Space 2022*; American Society of Civil Engineers: Reston, VA, USA, 2023; pp. 106–119. [CrossRef]
60. Algoryx. Real Physics Simulations—Fast. 2025. Available online: https://www.algoryx.se/ (accessed on 12 August 2025).
61. Schneider Company. Coefficient of Friction Reference Chart. 2025. Available online: https://www.schneider-company.com/coefficient-of-friction-reference-chart/ (accessed on 20 July 2025).
62. DuPont. *Kevlar Aramid Fiber Technical Guide*; Technical Report; DuPont: Wilmington, DE, USA, 2017.
63. Connolly, J.; Carrier, W.D. An Engineering Guide to Lunar Geotechnical Properties. In *Proceedings of the 2023 IEEE Aerospace Conference*; IEEE: Piscataway, NJ, USA, 2023.
64. Kanthal. Strip. 2025. Available online: https://www.kanthal.com/en/knowledge-hub/heating-material-knowledge/dimensions-and-properties2/strip/#nikrothal80 (accessed on 31 July 2025).
65. Reiss, P.; Hager, P.; Hoehn, A.; Rott, M.; Walter, U. Flowability of lunar regolith simulants under reduced gravity and vacuum in hopper-based conveying devices. *J. Terramech.* **2014**, *55*, 61–72. [CrossRef]
66. Detwiler, M.; Foong, C.S.; Stocklin, C. *Conceptual Design of Equipment to Excavate and Transport Regolith from the Lunar Maria*; Technical Report; NASA: Washington DC, USA, 1990.
67. Brown, I.; Burgoyne, C. The friction and wear of Kevlar 49 sliding against aluminium at low velocity under high contact pressures. *Wear* **1999**, *236*, 315–327. [CrossRef]
68. Asnani, V.; Delap, D.; Creager, C. The development of wheels for the Lunar Roving Vehicle. *J. Terramech.* **2009**, *46*, 89–103. [CrossRef]
69. Bell, J.F.; Maki, J.N.; Mehall, G.L.; Ravine, M.A.; Caplinger, M.A.; Bailey, Z.J.; Brylow, S.; Schaffner, J.A.; Kinch, K.M.; Madsen, M.B.; et al. The Mars 2020 Perseverance Rover Mast Camera Zoom (Mastcam-Z) Multispectral, Stereoscopic Imaging Investigation. *Space Sci. Rev.* **2021**, *217*, 24. [CrossRef]
70. Newill-Smith, D.; Shatts, J.; Dillon, R.P.; Karras, J.; Brinkman, A.; Backus, S.; Umali, A.; McCormick, R.; Fradet, L.; Laramee, J.; et al. Cold Operable Lunar Deployable Arm (COLDArm) System Development and Test. In *Proceedings of the 2023 IEEE Aerospace Conference*; IEEE: Piscataway, NJ, USA, 2023; pp. 1–19. [CrossRef]
71. GITAI. *GITAI Rover R1.5*; Datasheet; GITAI: Torrance, CA, USA, 2023.
72. Nakanose, S.; Nakamura-Messenger, K. GITAI USA: Providing Safe and Affordable Means of Labor in Space. In *Proceedings of the ASCEND 2023*; American Institute of Aeronautics and Astronautics: Reston, VA, USA, 2023. [CrossRef]
73. Howe, A.S.; Wilcox, B. Outpost assembly using the ATHLETE mobility system. In *Proceedings of the 2016 IEEE Aerospace Conference*; IEEE: Piscataway, NJ, USA, 2016; pp. 1–9. [CrossRef]

74. Howe, S.; Wilcox, B.H. High-capacity ATHLETE Offloader Mobility Constructor Concept for Human Planetary Surface Exploration. In *Proceedings of the ASCEND 2020*; American Institute of Aeronautics and Astronautics: Reston, VA, USA, 2020. [CrossRef]
75. Howe, S.; Nayar, H.; Wilcox, B. ATHLETE Offloader Limb as a High-capacity Crane. In *Proceedings of the ASCEND 2021*; American Institute of Aeronautics and Astronautics: Reston, VA, USA, 2021. [CrossRef]
76. Maki, J.; Thiessen, D.; Pourangi, A.; Kobzeff, P.; Litwin, T.; Scherr, L.; Elliott, S.; Dingizian, A.; Maimone, M. The Mars Science Laboratory Engineering Cameras. *Space Sci. Rev.* **2012**, *170*, 77–93. [CrossRef]
77. GITAI. *GITAI's Tech-Demo of Lunar Base Construction in a Mock Lunar Surface Environment*; Video; GITAI: Torrance, CA, USA, 2023. Available online: https://www.youtube.com/watch?v=4-hEH0dLMhI (accessed on 17 July 2025)
78. GITAI. *GITAI Inchworm Robot IN2*; Datasheet; GITAI: Torrance, CA, USA, 2023.
79. Goudsmit Magnetics. Goudsmit Magnetic Grippers. 2025. Available online: https://www.goudsmitmagnetics.com/uploads/pdf/selection_table_grippers_3156.pdf (accessed on 23 July 2025).
80. Goudsmit Magnetics. Feasible Magnetic Forces E-Grippers. 2025. Available online: https://www.goudsmitmagnetics.com/uploads/pdf/feasible_magnetic_forces_e_gripperV1_1_1680.pdf (accessed on 23 July 2025).
81. MDA. MDA Skymaker in the Making. 2025. Available online: https://mda.space/insights/mda-skymaker-in-the-making/ (accessed on 18 December 2025).
82. NVIDIA. NVIDIA Jetson Xavier. 2025. Available online: https://www.nvidia.com/en-us/autonomous-machines/embedded-systems/jetson-xavier-series/ (accessed on 23 July 2025).
83. NVIDIA. NVIDIA Jetson AGX Xavier Developer Kit. 2019. Available online: https://static6.arrow.com/aropdfconversion/78982174a186b77672854d211364da446dc3be6c/945-82972-0047-000.pdf?utm_source=chatgpt.com (accessed on 23 July 2025).
84. Motiv Space Systems. Bravo Motor Controller. 2023. Available online: https://motivss.com/wp-content/uploads/2021/09/Motiv9349BravoMotorControllerProductSheet.pdf (accessed on 22 July 2025).
85. Kaczmarzyk, M.; Musiał, M. Parametric Study of a Lunar Base Power Systems. *Energies* **2021**, *14*, 1141. [CrossRef]
86. Azur Space. SPACE Solar Cells. 2024. Available online: https://www.azurspace.com/en/products/space-products/ (accessed on 20 August 2024).
87. McClure, P.R.; Poston, D.I.; Gibson, M.A.; Mason, L.S.; Robinson, R.C. Kilopower Project: The KRUSTY Fission Power Experiment and Potential Missions. *Nucl. Technol.* **2020**, *206*, S1–S12. [CrossRef]
88. Calle, C.; Buhler, C.; McFall, J.; Snyder, S. Particle removal by electrostatic and dielectrophoretic forces for dust control during lunar exploration missions. *J. Electrost.* **2009**, *67*, 89–92. [CrossRef]
89. Kawamoto, H.; Miwa, T. Mitigation of lunar dust adhered to mechanical parts of equipment used for lunar exploration. *J. Electrost.* **2011**, *69*, 365–369. [CrossRef]
90. Calle, C.; Mackey, P.; Hogue, M.; Johansen, M.; Yim, H.; Delaune, P.; Clements, J. Electrodynamic Dust Shields on the International Space Station: Exposure to the space environment. *J. Electrost.* **2013**, *71*, 257–259. [CrossRef]
91. Colozza, A.J. *Small Lunar Base Camp and In Situ Resource Utilization Oxygen Production Facility Power System Comparison*; Technical Report; NASA: Washington DC, USA, 2020.
92. Saha, D.; Bazmohammadi, N.; Raya-Armenta, J.M.; Bintoudi, A.D.; Lashab, A.; Vasquez, J.C.; Guerrero, J.M. Space Microgrids for Future Manned Lunar Bases: A Review. *IEEE Open Access J. Power Energy* **2021**, *8*, 570–583. [CrossRef]
93. Surampudi, R.; Blosiu, J.; Bugga, R.; Brandon, E.; Smart, M.; Elliott, J.; Castillo, J.; Yi, T.; Lee, L.; Piszczor, M.; et al. *Energy Storage Technologies for Future Planetary Science Missions*; Technical Report; NASA: Washington DC, USA, 2017.
94. Garcia, C.P.; Chang, B.j.; Johnson, D.W.; Bents, D.J.; Scullin, V.J.; Jakupca, I.J. Round trip energy efficiency of NASA Glenn regenerative fuel cell system. In *Proceedings of the NHA Annual Hydrogen Conference 2006*; NASA: Washington DC, USA, 2006; number NASA/TM-2006-214054.
95. Mason, L.; Rucker, M. Common power and energy storage solutions to support lunar and Mars surface exploration missions. In *Proceedings of the International Astronautical Congress (IAC)*; NASA: Washington DC, USA, 2019; Number GRC-E-DAA-TN73896.
96. Bhasin, K.; Warner, J.; Anderson, L. Lunar Communication Terminals for NASA Exploration Missions: Needs, Operations Cocepts and Architectures. In Proceedings of the 26th International Communications Satellite Systems Conference (ICSSC), San Diego, CA, USA, 10–12 June 2008.
97. NASA. Chandrayaan 3. 2023. Available online: https://nssdc.gsfc.nasa.gov/nmc/spacecraft/display.action?id=2023-098A (accessed on 23 July 2025).
98. Kozman, R.; da Silva Curiel, A. Commercial Data Relay Services in the Cis-Lunar Environment with SSTL's Lunar Pathfinder. In Proceedings of the Small Satellite Conference, Logan, UT, USA, 5–10 August 2023.
99. Giordano, P.; Grenier, A.; Zoccarato, P.; Bucci, L.; Cropp, A.; Swinden, R.; Otero, D.G.; El-Dali, W.; Carey, W.; Duvet, L.; et al. Moonlight navigation service-how to land on peaks of eternal light. In Proceedings of the 72nd International Astronautical Congress (IAC), Dubai, United Arab Emirates, 25–29 October 2021; pp. 25–29.

100. Li, Y.; An, G.; Jia, Y.; Zhu, K.; Liu, C.; Chen, R.; Xu, J. Research on Lunar Communication Network Architecture and Protocol. In *Proceedings of the 2023 IEEE 15th International Conference on Advanced Infocomm Technology (ICAIT)*; IEEE: Piscataway, NJ, USA, 2023; pp. 91–96. [CrossRef]
101. NASA. *Radio Frequency and Optical Communication Link Trade Studies Between Earth, Deep Space Gateway and Lunar Surface*; Technical Report; NASA: Washington DC, USA, 2019.
102. Berkelman, P.; Chen, M.; Easudes, J.; Hancock, J.; Martin, M.C.; Mor, A.B.; Rollins, E.; Sharf, A.; Silberman, J.; Warren, T.; et al. *Design of a Day/Night Lunar Rover*; Tech. Rep.; Carnegie Mellon University: Pittsburgh, PA, USA, 1995.
103. Morgante, G.; Terenzi, L.; Desjonqueres, L.; Eccleston, P.; Bishop, G.; Caldwell, A.; Crook, M.; Drummond, R.; Hills, M.; Hunt, T.; et al. The thermal architecture of the ESA ARIEL payload at the end of phase B1. *Exp. Astron.* **2022**, *53*, 905–944. [CrossRef]
104. OMEGA. Polyimide Insulated Flexible Heaters. 2025. Available online: https://sea.omega.com/th/pptst/KHRA-KHLVA-KHA-SERIES.html (accessed on 31 July 2025).
105. Calle, C.; Chen, A.; Immer, C.; Csonka, M.; Hogue, M.; Snyder, S.; Rogriquez, M.; Margiotta, D. Dust Removal Technology Demonstration for a Lunar Habitat. In *Proceedings of the AIAA SPACE 2010 Conference & Exposition, Anaheim, CA, USA, 30 August–2 September 2010*; American Institute of Aeronautics and Astronautics: Reston, VA, USA, 2012. [CrossRef]
106. Mackey, P.J.; Johansen, M.R.; Olsen, R.C.; Raines, M.G.; Phillips, J.R.; Cox, R.E.; Hogue, M.D.; Pollard, J.R.S.; Calle, C.I. Electrodynamic Dust Shield for Space Applications. In *Proceedings of the Earth and Space 2016*; American Society of Civil Engineers: Reston, VA, USA, 2017; pp. 539–545. [CrossRef]
107. Johansen, M.R.; Dupuis, M.A.; Phillips, J.R., III; Malissa, J.D.; Wang, J.J.; Hogue, M.D.; Calle, C.I. Electrodynamic Dust Shield Testing on the Materials on International Space Station Experiment 11. In Proceedings of the International Astronautical Congress (IAC), Washington, DC, USA, 21–25 October 2019.
108. Tisdale, M.; Dulá, I.; Madrid, L.P.; Verkhovodova, P.; Pénot, J.; Coimbra, K.; Soldner, L.; Gupta, T.; Musuku, R.; Chung, S.J. Design of a Modular and Orientable Electrodynamic Shield for Lunar Dust Mitigation. In Proceedings of the AIAA SCITECH 2022 Forum, San Diego, CA, USA, 3–7 January 2022. [CrossRef]
109. Margiotta, D.V.; Peters, W.C.; Straka, S.A.; Rodriguez, M.; McKittrick, K.R.; Jones, C.B. The Lotus coating for space exploration: A dust mitigation tool. In *Proceedings of the Optical System Contamination: Effects, Measurements, and Control 2010*; Straka, S.A., Carosso, N., Eds.; International Society for Optics and Photonics; SPIE: Bellingham, WA, USA, 2010; Volume 7794, p. 77940I. [CrossRef]
110. Abel, P.B.; Anderson, M.D.; Blom, E.T.; Calle, C.; Dunlap, P.H.; Greenberg, P.S.; Fischer, D.G.; Howard, S.A.; Hurlbert, K.M.; Jordan, J.L.; et al. *Lunar Dust Mitigation: A Guide and Reference: (2021)*; Technical Report; NASA: Washington DC, USA, 2023.
111. Wohl, C.J.; Belcher, M.A.; Hopkins, J.W.; Connell, J.W. Topographical Modification of Materials for Lunar Dust Adhesion Mitigation. In Proceedings of the 40th Annual Lunar and Planetary Science Conference, Woodlands, TX, USA, 23–27 March 2009; p. 1121.
112. Wang, X.; Wang, W.; Shao, H.; Chao, S.; Zhang, H.; Tang, C.; Li, X.; Zhu, Y.; Zhang, J.; Zhang, X.; et al. Lunar Dust-Mitigation Behavior of Aluminum Surfaces with Multiscale Roughness Prepared by a Composite Etching Method. *ACS Appl. Mater. Interfaces* **2022**, *14*, 34020–34028. [CrossRef] [PubMed]
113. Delgado, I.R.; Handschuh, M.J. Preliminary assessment of seals for dust mitigation of mechanical components for lunar surface systems. In Proceedings of the 40th Aerospace Mechanisms Symposium, Cocoa Beach, FL, USA, 12–14 May 2010; Number E-17280.
114. Delgado, I.R.; Gaier, J.R.; Handschuh, M.; Panko, S.; Sechkar, E. *Performance Evaluation of an Actuator Dust Seal for Lunar Operation*; Technical Report; NASA: Washington DC, USA, 2013.
115. Bron Aerotech. BA 500BC PTFE Coated Fiberglass Beta Cloth. 2025. Available online: https://bronaerotech.com/products/ba-500bc-ptfe-coated-fiberglass-beta-cloth (accessed on 29 August 2025).
116. NASA. Ames Technical Standard ARC-STD-8070.1: Space Flight System Design and Environmental Test. 2018. Available online: https://www.nasa.gov/wp-content/uploads/2017/03/std8070.1.pdf (accessed on 14 March 2024).
117. Saha, D.; Bazmohammadi, N.; Raya-Armenta, J.M.; Bintoudi, A.D.; Lashab, A.; Vasquez, J.C.; Guerrero, J.M. Optimal Sizing and Siting of PV and Battery Based Space Microgrids Near the Moon's Shackleton Crater. *IEEE Access* **2023**, *11*, 8701–8717. [CrossRef]
118. Li, X.; Yu, W.; Wang, S.; Li, S.; Tang, H.; Li, Y.; Zheng, Y.; Tsang, K.T.; Ouyang, Z. Condition of Solar Radiation on the Moon. In *Moon*; Springer: Berlin/Heidelberg, Germany, 2012; pp. 347–365.
119. *ANSI/AIAA S-120A-2015*; Mass Properties Control for Space Systems. American Institute of Aeronautics and Astronautics: Reston, VA, USA, 2015.
120. European Space Agency. *MarsFAST: Assessment of an ESA Fast Mobility Mars Rover*; CDF Study Report ESA-CDF-148; European Space Agency: Paris, France, 2014.
121. Akin, D.L. Development and Testing of a Small Lunar Utility Rover. In *Proceedings of the AIAA Aviation Forum and ASCEND 2025, Las Vegas, NV, USA, 21–25 July 2025*; American Institute of Aeronautics and Astronautics: Reston, VA, USA, 2025. [CrossRef]

122. Pike, J. Advanced Missions Cost Model. 2005. Available online: https://www.globalsecurity.org/military/intro/reference/calc/AMCM.htm (accessed on 26 August 2025).
123. Leahy, F.B. SLS-SPEC-159, Cross-Program Design Specification for Natural Environments (DSNE). 2021. Available online: https://ntrs.nasa.gov/citations/20210024522 (accessed on 14 March 2024).
124. Budzyń, D.; Tuohy, E.; Garrivier, N.; Schild, T.; Cowley, A.; Cruise, R.; Adachi, M.; Zare-Behtash, H.; Cammarano, A. Lunar dust: Its impact on hardware and mitigation technologies. In *Proceedings of the 46th Aerospace Mechanisms Symposium*; Mechanisms Education Association: Tujunga, CA, USA, 2022; Volume 287.
125. Benaroya, H. Chapter 3: The lunar environment. In *Building Habitats on the Moon: Engineering Approaches to Lunar Settlements*; Springer International Publishing: Cham, Switzerland, 2018; pp. 42–84.

Disclaimer/Publisher's Note: The statements, opinions and data contained in all publications are solely those of the individual author(s) and contributor(s) and not of MDPI and/or the editor(s). MDPI and/or the editor(s) disclaim responsibility for any injury to people or property resulting from any ideas, methods, instructions or products referred to in the content.